Cell Reports

Article

Pyruvate dehydrogenase fuels a critical citrate pool that is essential for Th17 cell effector functions

Graphical abstract

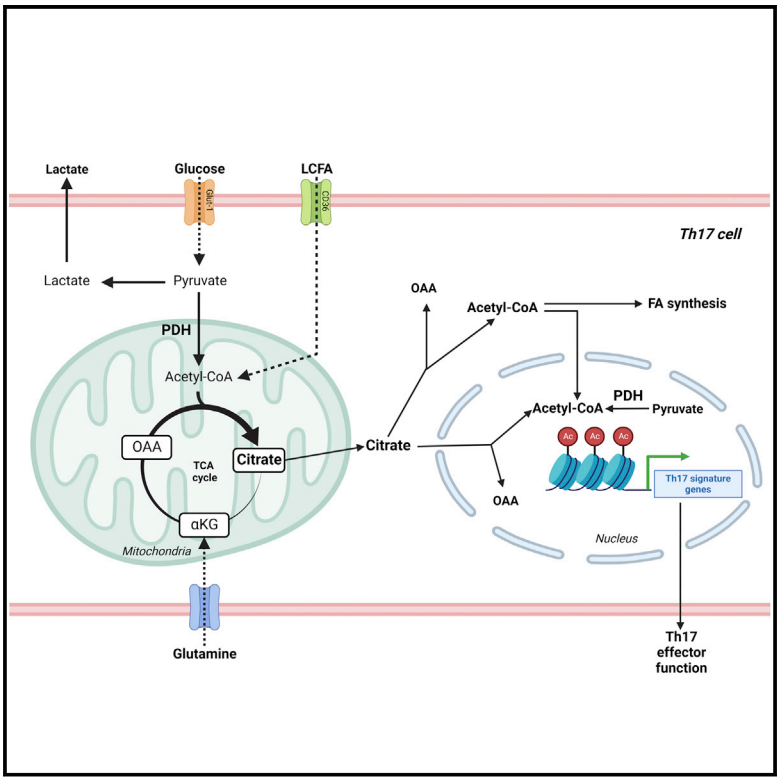

Highlights

- PDH-ablation in T cells lowers Th17 cell-mediated autoimmunity
- PDH is essential for the pathogenic function of Th17 cells and IL-17 production
- PDH fuels a citrate pool controlling glycolysis, glutaminolysis, and lipids
- PDH controls histone acetylation and Th17 cell gene transcription

Authors

Leticia Soriano-Baguet, Melanie Grusdat, Henry Kurniawan, ..., Karsten Hiller, Johannes Meiser, Dirk Brenner

Correspondence

dirk.brenner@lih.lu

In brief

Pyruvate dehydrogenase (PDH) connects glycolysis with the mitochondrial tricarboxylic acid (TCA) cycle. Soriano-Baguet et al. show that PDH directs a glucose-derived citrate pool that coordinates the central carbon metabolism and histone acetylation and is essential for Th17 cell function.

Soriano-Baguet et al., 2023, Cell Reports *42*, 112153
March 28, 2023
https://doi.org/10.1016/j.celrep.2023.112153

CellPress

Cell Reports

CellPress
OPEN ACCESS

Article

Pyruvate dehydrogenase fuels a critical citrate pool that is essential for Th17 cell effector functions

Leticia Soriano-Baguet,[1,2] Melanie Grusdat,[1,2] Henry Kurniawan,[1,2] Mohaned Benzarti,[3,4] Carole Binsfeld,[1,2] Anouk Ewen,[1,2] Joseph Longworth,[1,2] Lynn Bonetti,[1,2] Luana Guerra,[1,2] Davide G. Franchina,[1,2] Takumi Kobayashi,[1,2] Veronika Horkova,[1,2] Charlène Verschueren,[1,2] Sergio Helgueta,[5,6] Deborah Gérard,[6] Tushar H. More,[7] Antonia Henne,[7] Catherine Dostert,[1,2] Sophie Farinelle,[1,2] Antoine Lesur,[8] Jean-Jacques Gérardy,[5,9] Christian Jäger,[10] Michel Mittelbronn,[4,5,9,10,11,12] Lasse Sinkkonen,[6] Karsten Hiller,[7] Johannes Meiser,[3,8] and Dirk Brenner[1,2,13,14,*]

[1]Experimental and Molecular Immunology, Department of Infection and Immunity, Luxembourg Institute of Health, Esch-sur-Alzette, Luxembourg

[2]Immunology and Genetics, Luxembourg Centre for Systems Biomedicine, University of Luxembourg, 7, Avenue des Hauts Fourneaux, Esch-sur-Alzette, Luxembourg

[3]Cancer Metabolism Group, Department of Cancer Research, Luxembourg Institute of Health, Luxembourg, Luxembourg

[4]Faculty of Science, Technology, and Medicine, University of Luxembourg, Esch-sur-Alzette, Luxembourg

[5]Luxembourg Center of Neuropathology, 3555 Dudelange, Luxembourg

[6]Epigenetics Team, Systems Biology Group, Department of Life Sciences and Medicine, University of Luxembourg, Belvaux, Luxembourg

[7]Department of Bioinformatics and Biochemistry, Braunschweig Integrated Center of Systems Biology, Technische Universität Braunschweig, Rebenring 56, 38106 Braunschweig, Germany

[8]Metabolomics Platform, Department of Cancer Research, Luxembourg Institute of Health, Luxembourg, Luxembourg

[9]National Center of Pathology, Laboratoire National de Santé (LNS), Dudelange, Luxembourg

[10]Luxembourg Center for Systems Biomedicine, University of Luxembourg, 4362 Esch-sur-Alzette, Luxembourg

[11]Department of Life Sciences and Medicine, University of Luxembourg, Esch-sur-Alzette, Luxembourg

[12]Department of Cancer Research, Luxembourg Institute of Health, 1526 Luxembourg, Luxembourg

[13]Odense Research Center for Anaphylaxis, Department of Dermatology and Allergy Center, Odense University Hospital, University of Southern Denmark, Odense, Denmark

[14]Lead contact

*Correspondence: dirk.brenner@lih.lu

https://doi.org/10.1016/j.celrep.2023.112153

SUMMARY

Pyruvate dehydrogenase (PDH) is the central enzyme connecting glycolysis and the tricarboxylic acid (TCA) cycle. The importance of PDH function in T helper 17 (Th17) cells still remains to be studied. Here, we show that PDH is essential for the generation of a glucose-derived citrate pool needed for Th17 cell proliferation, survival, and effector function. *In vivo*, mice harboring a T cell-specific deletion of PDH are less susceptible to developing experimental autoimmune encephalomyelitis. Mechanistically, the absence of PDH in Th17 cells increases glutaminolysis, glycolysis, and lipid uptake in a mammalian target of rapamycin (mTOR)-dependent manner. However, cellular citrate remains critically low in mutant Th17 cells, which interferes with oxidative phosphorylation (OXPHOS), lipid synthesis, and histone acetylation, crucial for transcription of Th17 signature genes. Increasing cellular citrate in PDH-deficient Th17 cells restores their metabolism and function, identifying a metabolic feedback loop within the central carbon metabolism that may offer possibilities for therapeutically targeting Th17 cell-driven autoimmunity.

INTRODUCTION

T cells are essential for adaptive immune responses, and T helper 17 (Th17) cells are the $CD4^+$ subset that protects the host against extracellular bacteria and fungi.[1] However, Th17 cells are also linked to autoimmune diseases such as multiple sclerosis and rheumatoid arthritis.[2,3] Th17 cells are defined by their expression of RORγT and the ability to produce interleukin-17 (IL-17).[3,4]

All T cells adapt their metabolism according to their energy demands.[5,6] Upon activation, $CD4^+$ T cells switch from mitochondrial metabolism (i.e., the tricarboxylic acid [TCA] cycle, oxidative phosphorylation [OXPHOS], and fatty acid β-oxidation) to glycolysis and glutaminolysis to generate ATP and biosynthetic precursors, a process dubbed "metabolic reprogramming." This metabolic rewiring then supports the molecular signaling needed for T cell proliferation and effector functions.[7–10] However, each Th cell subset shows features during

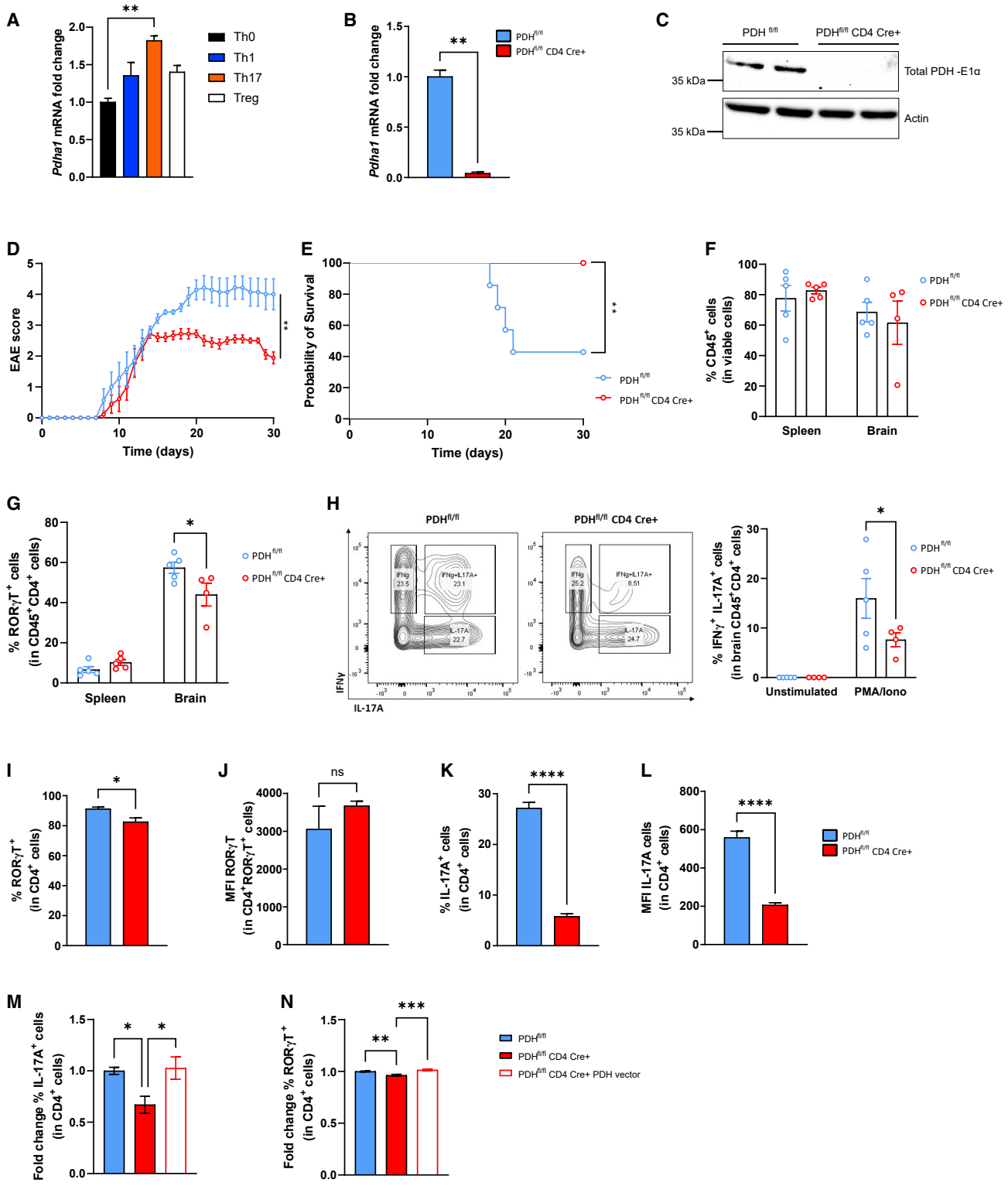

Figure 1. *Pdh* ablation in T cells protects mice from severe EAE and impairs IL-17 production

(A) qPCR determination of fold change in *Pdha1* mRNA levels in the indicated wild-type (WT) T cell subsets that were induced to differentiate *in vitro* as described in STAR Methods. ΔΔCt values were normalized to Tbp expression. Data are mean ± SEM (n = 3) and representative of 2 trials.

(B) qPCR determination as in (A) of *Pdha1* mRNA levels in total CD4$^+$ T cells that were isolated from spleen and lymph nodes of control (PDH$^{fl/fl}$) and PDH-deficient (PDH$^{fl/fl}$CD4 Cre+) mice and activated *in vitro* for 24 h with anti-CD3/anti-CD28 antibodies. Data are mean ± SEM (n = 3) and representative of 2 trials.

(legend continued on next page)

metabolic reprogramming that are specific to that subset,[11] and the details of this process in Th17 cells are not fully understood.

The mitochondrial pyruvate dehydrogenase (PDH) complex regulates the flux of cytoplasmic glucose into the TCA cycle.[12] PDH catalyzes the conversion of glucose-derived pyruvate into acetyl coenzyme A (CoA), which then condenses with oxaloacetate (OAA) to generate citrate.[1,13] Citrate enters the TCA cycle to produce the reducing equivalents necessary for ATP production via OXPHOS. In addition, citrate is transported out of the mitochondria into the cytoplasm and can even enter the nucleus, where it is converted back into acetyl-CoA and OAA by ATP-citrate lyase (ACLY).[11,14–17] Cytoplasmic acetyl-CoA drives lipid synthesis, whereas nuclear acetyl-CoA participates in histone acetylation regulating cell-type-specific gene expression.[18–20]

In this study, we show in mice that PDH plays a crucial role in metabolic adaptation and functions of Th17 cells. Mechanistically, genetic ablation of PDH reduces cellular citrate below a threshold level, which triggers metabolic alterations such as increased glycolysis, glutaminolysis, and fatty acid uptake. These changes can sustain the survival and proliferation of Th17 cells but not their effector functions, either *in vitro* or *in vivo*. PDH-synthesized citrate was found to be essential for histone acetylation and subset-specific gene expression in Th17 cells. Consequently, replenishing the citrate pool by exogenous addition of acetate reinstated normal Th17 cell metabolism and function. Our results demonstrate the importance of PDH in the generation of a critical citrate pool that is indispensable for maintaining Th17 cell function.

RESULTS

Loss of *Pdh* in T cells protects mice from severe experimental autoimmune encephalomyelitis (EAE)

The PDH complex is composed of the PDH-E1α subunit, which is encoded by the *Pdha1* gene, and the PDH-E1β subunit, encoded by *Pdhb*. The PDH-E1α subunit catalyzes the rate-limiting step of pyruvate conversion into acetyl-CoA, whereas the PDH-E1β subunit has no catalytic activity in the absence of PDH-E1α.[21] To investigate PDH's importance in T cell metabolic adaptation, we analyzed *Pdha1* mRNA levels in various CD4$^+$ Th subsets induced to differentiate *in vitro*. Th17 cells showed greater *Pdha1* expression than Th0, Th1, or regulatory T (Treg) cells (Figure 1A). We then crossed CD4 Cre+ mice with Pdha1^{flox8} mice to generate a mutant mouse strain (PDH$^{fl/fl}$ CD4 Cre+) in which T cells did not express *Pdha1* mRNA or protein (Figures 1B and 1C) but continued to express *Pdhb1* mRNA encoding the inactive PDH-E1β subunit (Figure S1A).

Next, we induced EAE, a mouse model of multiple sclerosis known to depend on Th17 cells,[2] in control (PDH$^{fl/fl}$) and PDH$^{fl/fl}$ CD4 Cre+ mice. PDH$^{fl/fl}$ CD4 Cre+ mice showed significant reductions in disease burden and mortality compared with littermate controls (Figures 1D and 1E). T cells isolated from brains and spleens of control and PDH$^{fl/fl}$ CD4 Cre+ mice on day 14 post EAE induction showed comparable percentages and numbers of CD45$^+$ infiltrating cells (Figures 1F and S1B). However, while brains of PDH$^{fl/fl}$ CD4 Cre+ mice showed normal infiltration of Tbet$^+$ Th1 cells, the percentages of infiltrating RORγT$^+$ Th17 cells and CD25$^+$Foxp3$^+$ Treg cells were reduced (Figures 1G, S1C, and S1D). We then analyzed Th17 cell function by measuring interferon γ (IFNγ) and IL-17A production by CD45$^+$CD4$^+$ cells that were isolated from mouse brains and stimulated *in vitro* with phorbol 12-myristate 13-acetate (PMA)/ionomycin. The IFNγ^+IL-17A$^+$ Th17 cell subset deemed to be pathogenic was significantly decreased in proportion in PDH$^{fl/fl}$ CD4 Cre+ brains (Figure 1H), whereas the frequencies of IFNγ^+IL-17A$^-$ and IFNγ^-IL-17A$^+$ CD4$^+$ T cells were unaffected (Figures S1E and S1F). Thus, PDH is critical for Th17 cell function *in vivo*.

To gain mechanistic insight into PDH's role in Th17 cells, we induced naive CD4$^+$ T cells isolated from spleens and lymph nodes of control and PDH$^{fl/fl}$ CD4 Cre+ mice to differentiate into Th17 cells *in vitro* by exposing them to anti-CD3/CD28 antibodies plus IL-6 and transforming growth factor β (TGF-β).[4,22] PDH-deficient Th17 cells showed only marginally decreased RORγT expression but markedly impaired IL-17 production

(C) Representative immunoblot to detect total PDH-E1α protein in total CD4$^+$ T cells that were isolated from spleen and lymph nodes of two PDH$^{fl/fl}$ and two PDH$^{fl/fl}$ CD4 Cre+ mice and activated *in vitro* as in (B). Actin, loading control. Data are representative of 4 mice/genotype.
(D and E) EAE clinical scores (D) and survival (E) of PDH$^{fl/fl}$ (n = 7) and PDH$^{fl/fl}$ CD4 Cre+ (n = 9) mice 30 days post induction. Data in (D) are mean ± SEM.
(F) Flow cytometry analysis (FCA) of frequencies of CD45$^+$ cells among viable cells isolated from spleens and brains of PDH$^{fl/fl}$ and PDH$^{fl/fl}$ CD4 Cre+ mice on day 14 post EAE induction. Data are mean ± SEM (n = 4–5/group).
(G) Intracellular FCA of frequencies of RORγT$^+$ cells among viable CD45$^+$CD4$^+$ cells isolated from spleens and brains of the mice in (F). Data are mean ± SEM (n = 4–5/group).
(H) Left: representative contour plots of intracellular staining of IL-17A and IFNγ among viable CD45$^+$CD4$^+$ cells isolated from the brains of the mice in (F) (n = 4/genotype). Cells were stimulated *in vitro* with PMA/calcium ionophore/Brefeldin A (PMA/Iono) for 5 h before staining. Right: quantification of frequencies of the IFNγ^+IL-17A$^+$ cells in the left panel. Data are mean ± SEM (n = 4–5/group).
(I and J) Naive T cells were isolated from spleen and lymph nodes of PDH$^{fl/fl}$ and PDH$^{fl/fl}$ CD4 Cre+ mice and differentiated *in vitro* into Th17 cells for 3 days. Results shown are intracellular FCA of frequencies of RORγT$^+$ cells (I) and quantification of RORγT mean fluorescence intensity (MFI) (J), gated on viable CD4$^+$RORγT$^+$ cells. Data are mean ± SEM (n = 3) and representative of 4 trials.
(K and L) Naive T cells were isolated from spleen and lymph nodes of PDH$^{fl/fl}$ and PDH$^{fl/fl}$ CD4 Cre+ mice and differentiated *in vitro* into Th17 cells for 3 days. Results shown are intracellular FCA of frequencies of IL-17A$^+$ cells after 5-h stimulation with PMA/Iono (K) and quantification of IL-17A MFI (L), gated on viable CD4$^+$ cells. Data are mean ± SEM (n = 3) and representative of 4 trials.
(M and N) Naive T cells were isolated from spleen and lymph nodes of PDH$^{fl/fl}$ and PDH$^{fl/fl}$ CD4 Cre+ mice and differentiated *in vitro* into Th17 cells for 3 days. On day 1, Th17 cells were infected with a control- or PDH-expressing retroviral vector. Results shown are intracellular FCA of frequencies of IL-17A$^+$ cells after 5-h stimulation with PMA/Iono (M) and intracellular FCA of frequencies of RORγT$^+$ cells gated on viable CD4$^+$ cells (N). Data are mean ± SEM (n = 9) and pooled from 3 trials.
The p values are determined by unpaired two-tailed Student's t test or one- or two-way ANOVA where appropriate. Correction for multiple comparisons was performed using the Tukey test. *p < 0.05, **p < 0.01, ***p < 0.001, ****p < 0.0001).

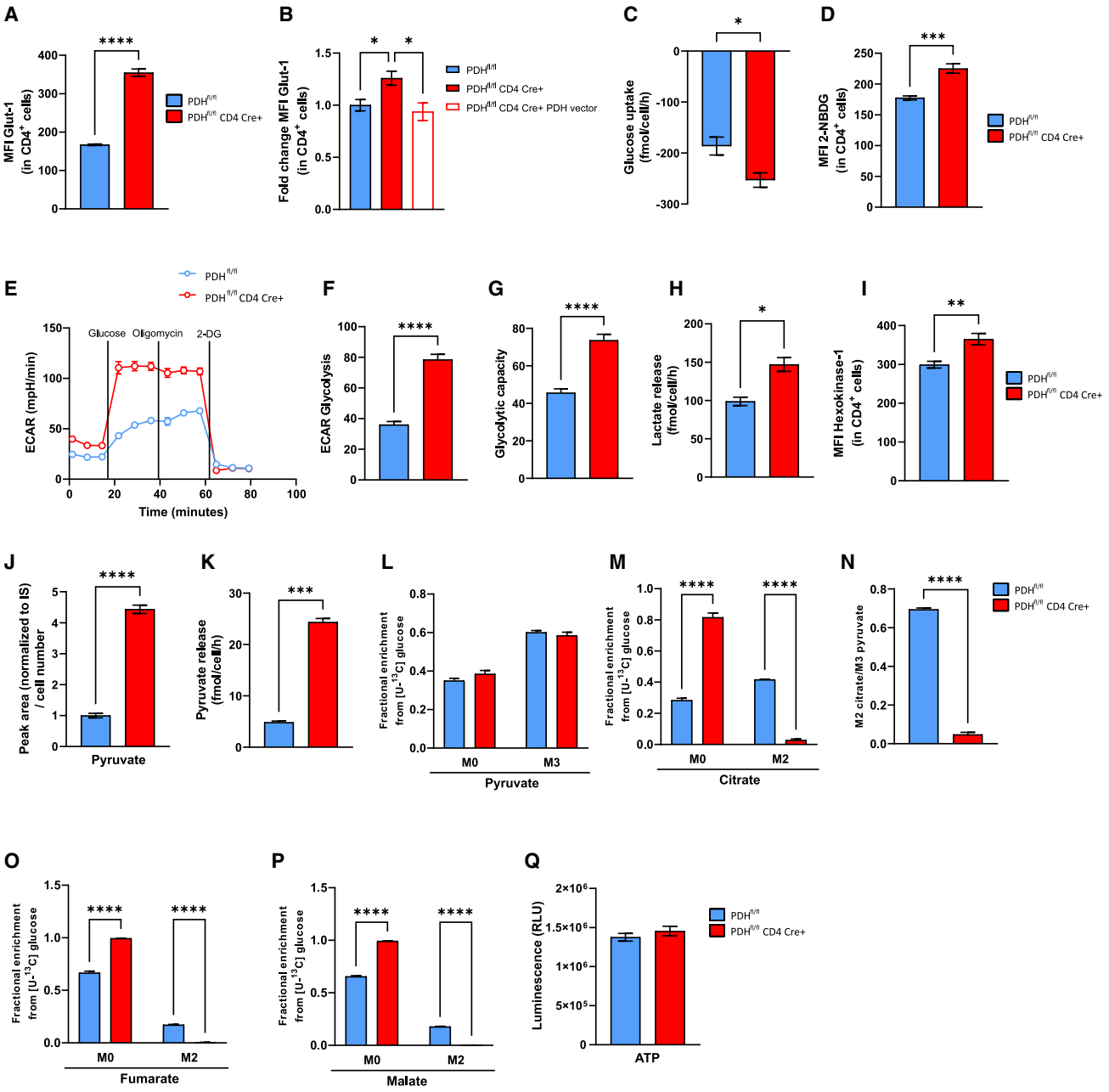

Figure 2. PDH in T cells is essential for glucose metabolism

(A) Quantification of Glut-1 MFI in PDH$^{fl/fl}$ and PDH$^{fl/fl}$ CD4 Cre+ Th17 cells, gated on viable CD4$^+$ cells. Data are mean ± SEM (n = 3) and representative of 3 trials.

(B) Naive T cells were isolated from spleen and lymph nodes of PDH$^{fl/fl}$ and PDH$^{fl/fl}$ CD4 Cre+ mice and differentiated *in vitro* into Th17 cells for 3 days. On day 1, Th17 cells were infected with a control or PDH-expressing retroviral vector as in Figure 1M. Results shown are quantification of Glut-1 MFI, gated on viable CD4$^+$ cells. Data are mean ± SEM (n = 6) and representative of 3 trials.

(C) YSI quantification of glucose uptake from the culture medium of PDH$^{fl/fl}$ and PDH$^{fl/fl}$ CD4 Cre+ Th17 cells. Data are mean ± SEM (n = 3) and representative of 2 trials.

(D) Quantification of 2-NBDG MFI in PDH$^{fl/fl}$ and PDH$^{fl/fl}$ CD4 Cre+ Th17 cells, gated on viable CD4$^+$ cells. Data are mean ± SEM (n = 3) and representative of 3 trials.

(E) Representative Seahorse ECAR plot for PDH$^{fl/fl}$ and PDH$^{fl/fl}$ CD4 Cre + Th17 cells. Data are mean ± SEM (n = 3) and representative of 3 trials.

(F and G) Quantification of Seahorse determinations of glycolytic capacity (F) and glycolysis (G) in PDH$^{fl/fl}$ and PDH$^{fl/fl}$ CD4 Cre+ Th17 cells. Data are mean ± SEM (n = 3) and representative of 3 trials.

(H) YSI quantification of lactate released into the culture medium of PDH$^{fl/fl}$ and PDH$^{fl/fl}$ CD4 Cre+ Th17 cells. Data are mean ± SEM (n = 3) and representative of 2 trials.

(legend continued on next page)

(Figures 1I–1L and S1G). Importantly, upon PDH re-expression via retroviral transduction of a PDH-expressing vector (Figure S1H), IL-17A production was restored to control levels in PDH-deficient Th17 cells (Figure 1M). The slight reduction in RORγT expression in PDH-deficient Th17 cells could also be restored by PDH re-expression (Figure 1N). In contrast, Th1 cell differentiation, effector function, or Treg induction were not affected by PDH ablation (Figures S1I–S1K). Thus, Th17 cell effector functions, but not differentiation per se, depend on PDH.

PDH is essential for regulation of glucose metabolism in Th17 cells

We hypothesized that PDH loss in Th17 cells would trigger a metabolic shift impeding their function. Flow cytometry analysis (FCA) revealed that expression of Glut-1, the major glucose transporter in T cells,[23] was increased in PDH-deficient Th17 cells compared with controls and restored to wild-type levels upon PDH re-expression (Figures 2A and 2B). This result aligned with the PDH-deficient cells' elevated glucose uptake as determined by mass spectrometry (MS) and enhanced uptake of the fluorescent glucose analog 2-(N-(7-nitrobenz-2-oxa-1,3-diazol-4-yl) amino)-2-deoxyglucose (2-NBDG)[24] (Figures 2C and 2D). Extracellular flux analyses confirmed significantly increased glycolysis and glycolytic capacity in PDH-deficient Th17 cells that were associated with heightened lactate release (Figures 2E–2H). Furthermore, the mutant cells exhibited increased expression of hexokinase-1, which catalyzes the irreversible conversion of glucose to glucose-6-phosphate,[25] as well as enhanced intracellular concentrations and release of pyruvate, the end product of glycolysis (Figures 2I–2K). These data pointed to increased flux through glycolysis that, because PDH-deficient Th17 cells cannot further metabolize pyruvate, resulted in pyruvate release into the culture medium.

Despite the above, glycolytic flux analysis using an exogenous ^{13}C-glucose tracer[26] revealed no difference in the contribution of ^{13}C-glucose to pyruvate (M3 label) between control and PDH-deficient Th17 cells (Figure 2L). This result further substantiated our findings that glycolytic activity was increased but that glucose flux through glycolysis itself remained unchanged in the absence of PDH. In contrast, there was minimal ^{13}C-glucose incorporation into citrate (M2 label) (Figure 2M). We then calculated the ratio of M2 citrate/M3 pyruvate as a proxy for measuring PDH activity and observed that this ratio was drastically reduced in PDH-deficient Th17 cells (Figure 2N). ^{13}C-glucose incorporation into other TCA metabolites, such as fumarate and malate (M2 label), was also minimal in PDH-deficient Th17 cells (Figures 2O and 2P). Nonetheless, despite this lack of glucose entering the TCA cycle, PDH-deficient Th17 cells generated normal amounts of energy in the form of ATP (Figure 2Q). These data suggested that these mutant cells used an alternative source of carbon for energy production.

PDH-derived acetyl-CoA is essential for a functioning TCA cycle in Th17 cells

Glutamine can replenish the TCA cycle at the stage of α-ketoglutarate (αKG),[27] and we observed that glutamine uptake was increased in PDH-deficient Th17 cells (Figure 3A). In accordance, ^{13}C-glutamine incorporation into TCA metabolites such as fumarate and malate (M4 label) was elevated in PDH-deficient Th17 cells (Figures 3B and 3C). However, we did not detect an increased flux to citrate, either by oxidative (M4 label) or reductive (M5 label) glutamine metabolism (Figures 3D and 3E). These results bolstered our hypothesis that citrate synthesis in Th17 cells requires PDH-generated acetyl-CoA.

RNA sequencing (RNA-seq) analysis revealed a significant sample distance between the transcriptomes of wild-type and PDH-deficient Th17 cells (Figure S2A). Moreover, in line with their decreased glucose flux into the TCA cycle, we observed an overall reduction in expression of TCA cycle enzymes in mutant Th17 cells compared with controls (Figure S2B). Thus, without PDH-E1α, Th17 cells cannot convert pyruvate into acetyl-CoA to feed into the TCA cycle, and this deficit compromises Th17 cell effector functions. Indeed, in accordance with their reduced expression of TCA enzymes, PDH-deficient Th17 cells showed deficits in basal oxygen consumption rate (OCR), OCR-dependent ATP production, and spare respiratory capacity (Figures 3F–3J).

Because the contributions of glucose- and glutamine-derived carbons to the TCA cycle were altered, we used MS to measure total intracellular levels of TCA metabolites in control and PDH-deficient Th17 cells. In line with our previous results, we observed that absolute levels of αKG, fumarate, and malate were reduced and citrate levels were minimal in PDH-deficient Th17 cells (Figures 3K–3N). Thus, an absence of PDH in Th17 cells drastically alters the central oxidative metabolism, prevents glucose flux into the TCA cycle, and impairs citrate formation so that it cannot be replenished by glutamine.

PDH ablation induces fatty acid uptake by Th17 cells

Citrate is an essential metabolite for several processes, including *de novo* lipid synthesis. In this context, citrate exits the

(I) Quantification of hexokinase-1 MFI in PDH$^{fl/fl}$ and PDH$^{fl/fl}$ CD4 Cre+ Th17 cells, gated on viable CD4$^+$ cells. Data are mean ± SEM (n = 3) and representative of 2 trials.
(J) Quantification of intracellular pyruvate in PDH$^{fl/fl}$ and PDH$^{fl/fl}$ CD4 Cre+ Th17 cells. Data are mean ± SEM (n = 3) and representative of 2 trials.
(K) Gas chromatography (GC)-MS quantification of pyruvate release into the culture medium of PDH$^{fl/fl}$ and PDH$^{fl/fl}$ CD4 Cre + Th17 cells. Data are mean ± SEM (n = 3) and representative of 2 trials.
(L and M) Mass isotopomer distribution (MID) of M0 and M3 pyruvate (L) and M0 and M2 citrate (M) in PDH$^{fl/fl}$ and PDH$^{fl/fl}$ CD4 Cre+ Th17 cells incubated for 24 h with [U-$^{13}C_6$]-glucose. Data are mean ± SEM (n = 3) and representative of 2 trials.
(N) PDH activity ratio (M2 citrate/M3 pyruvate) in the cells in (L) and (M). Data are mean ± SEM (n = 3) and representative of 2 trials.
(O and P) MID of M0 and M2 fumarate (O) and M0 and M2 malate (P) in PDH$^{fl/fl}$ and PDH$^{fl/fl}$ CD4 Cre+ Th17 cells incubated for 24 h with [U-$^{13}C_6$]-glucose. Data are mean ± SEM (n = 3) and representative of 2 trials.
(Q) Luminescence determination of ATP in PDH$^{fl/fl}$ and PDH$^{fl/fl}$ CD4 Cre+ Th17 cells. Data are mean ± SEM (n = 3) and representative of 2 trials.
The p values are determined by unpaired two-tailed Student's t test or one- or two-way ANOVA where appropriate. Correction for multiple comparisons was performed using the Tukey test. *p < 0.05, **p < 0.01, ***p < 0.001, ****p < 0.0001.

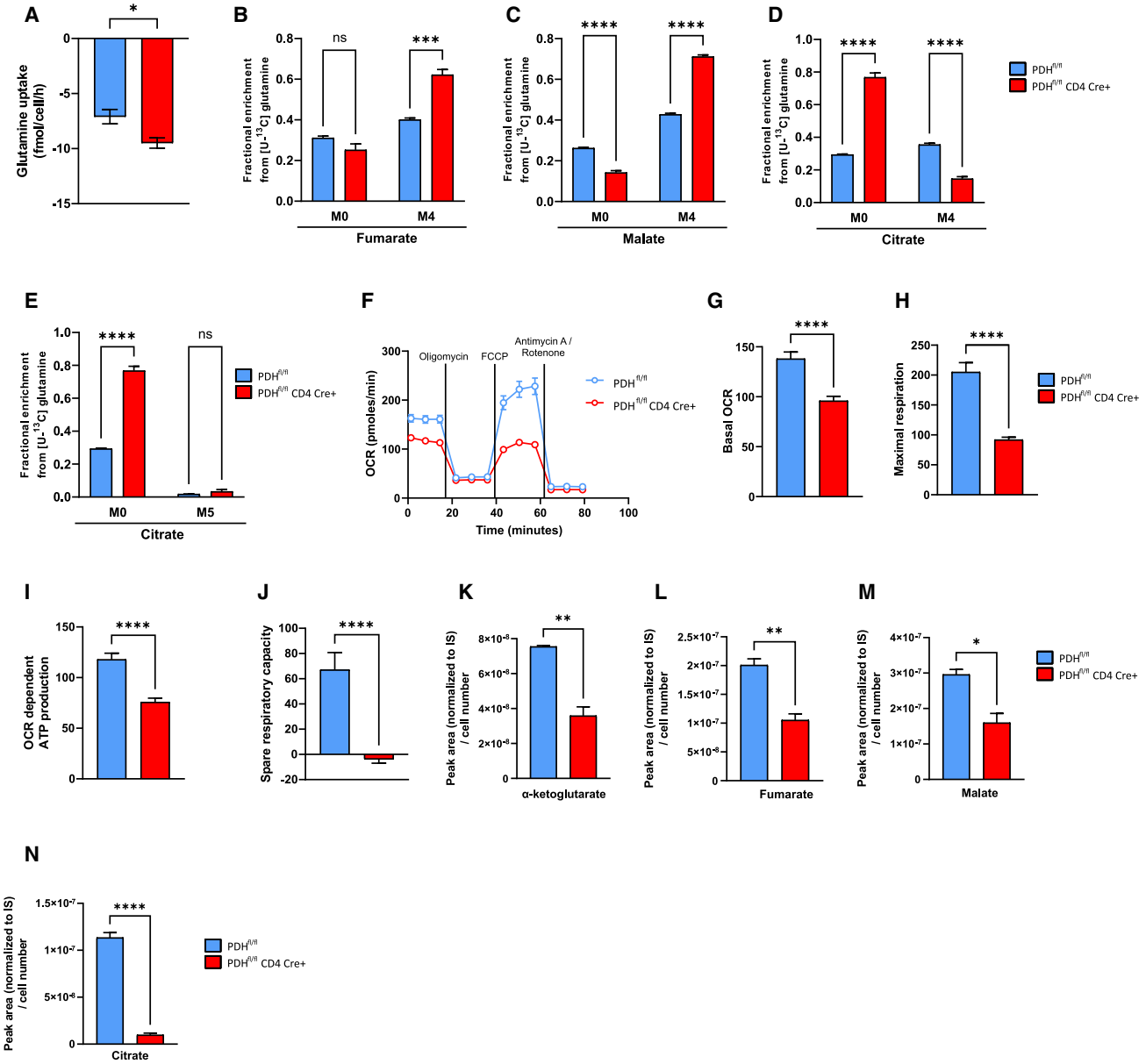

Figure 3. Glutamine metabolism is altered upon PDH ablation

(A) YSI quantification of glutamine uptake from the culture medium of $PDH^{fl/fl}$ and $PDH^{fl/fl}$CD4Cre+ Th17 cells. Data are mean ± SEM (n = 3) and representative of 2 trials.

(B–E) MID of M0 and M4 fumarate (B), M0 and M4 malate (C), M0 and M4 citrate (D), and M0 and M5 citrate (E) in $PDH^{fl/fl}$ and $PDH^{fl/fl}$ CD4 Cre+ Th17 cells incubated for 24 h with [U-$^{13}C_5$]-glutamine. Data are mean ± SEM (n = 3) and representative of 2 trials.

(F) Representative Seahorse OCR plot of $PDH^{fl/fl}$ and $PDH^{fl/fl}$ CD4 Cre+ Th17 cells. Data are mean ± SEM (n = 3) and representative of 3 trials.

(G–J) Quantification of Seahorse determinations of basal OCR (G), maximal respiration (H), OCR-dependent ATP (I), and spare respiratory capacity (J) in $PDH^{fl/fl}$ and $PDH^{fl/fl}$ CD4 Cre+ Th17 cells. Data are mean ± SEM (n = 3) and representative of 3 trials.

(K–N) Quantification of intracellular αKG (K), fumarate (L), malate (M), and citrate (N) in $PDH^{fl/fl}$ and $PDH^{fl/fl}$ CD4 Cre+ Th17 cells. Data are mean ± SEM (n = 3) and representative of 2 trials.

The p values are determined by unpaired two-tailed Student's t test or two-way ANOVA where appropriate. Correction for multiple comparisons was performed using the Tukey test. *p < 0.05, **p < 0.01, ***p < 0.001, ****p < 0.0001.

mitochondria and enters the cytoplasm, where it is converted by ACLY into OAA and acetyl-CoA, which is used for fatty acid synthesis.[14,16,19] We first measured total levels of fatty acid octadecenoic acid in control and PDH-deficient Th17 cells and observed them to be similar (Figure 4A). However, ^{13}C-glucose and ^{13}C-glutamine tracing revealed almost no contribution of these carbon sources to octodecenoic acid synthesis in PDH-deficient Th17 cells (Figures 4B, S3A, and S3B). Thus, the

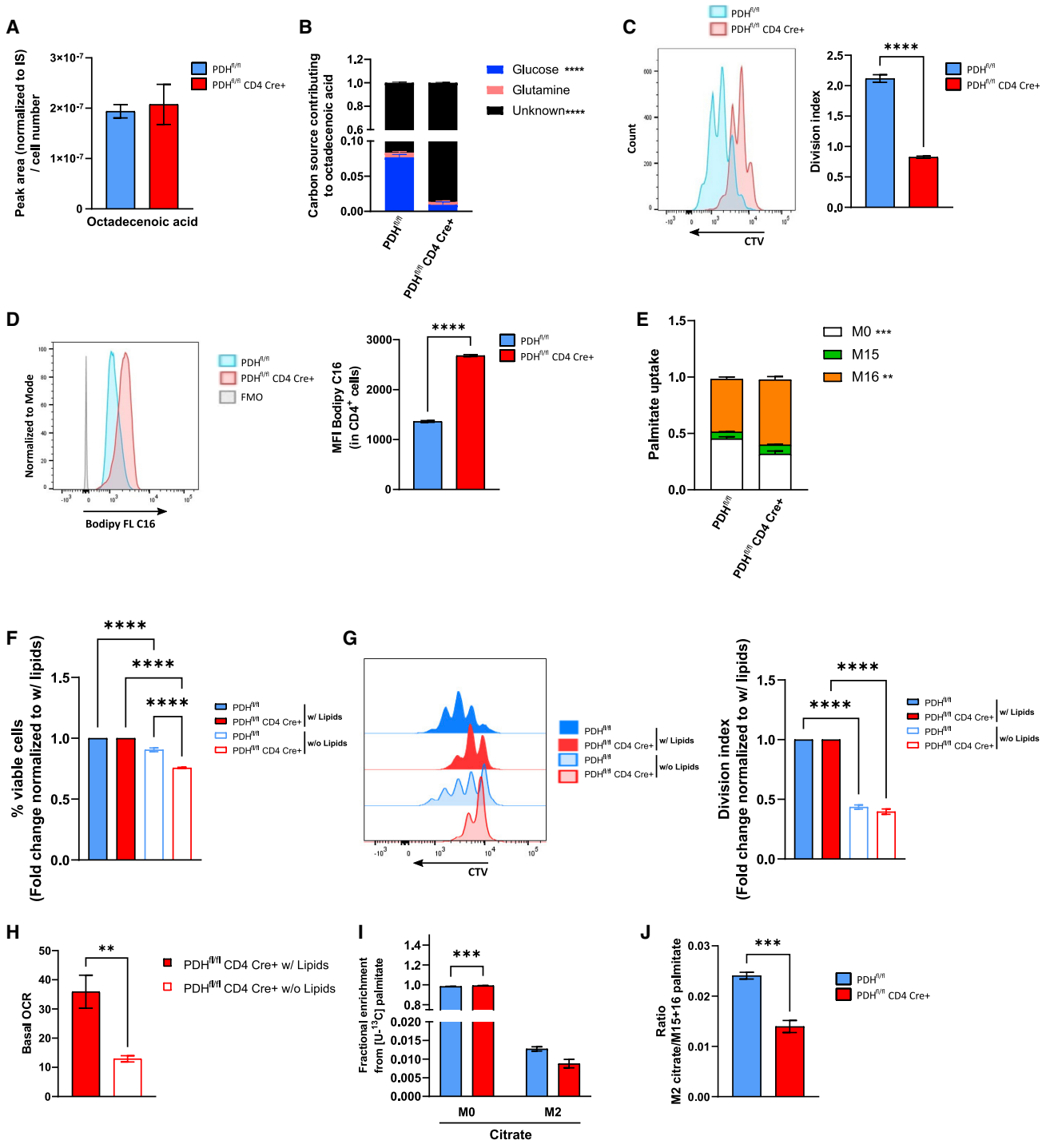

Figure 4. Ablation of PDH in Th17 cells induces fatty acid metabolism

(A) GC-MS quantification of intracellular octadecenoic acid in PDH$^{fl/fl}$ and PDH$^{fl/fl}$ CD4 Cre+ Th17 cells. Data are mean ± SEM (n = 3) and representative of 2 trials.

(B) Distribution of carbon sources contributing to octadecenoic acid in PDH$^{fl/fl}$ and PDH$^{fl/fl}$ CD4 Cre+ Th17 cells. Data are mean ± SEM (n = 3) and representative of 2 trials.

(C) Left: representative FCA of the proliferation of CellTrace Violet (CTV)-labeled PDH$^{fl/fl}$ and PDH$^{fl/fl}$ CD4 Cre+ Th17 cells. Right: fold change of the division index of the Th17 cells in the left panel. Data are mean ± SEM (n = 3) and representative of 3 trials.

(D) Left: representative FCA of BODIPY FL C16-labeled PDH$^{fl/fl}$ and PDH$^{fl/fl}$ CD4 Cre+ Th17 cells and fluorescence minus one (FMO) of unlabeled Th17 cells. Right: Quantification of BODIPY FL C16 MFI in the Th17 cells in the left panel, gated on viable CD4$^+$ cells. Data are mean ± SEM (n = 3) and representative of 3 trials.

(legend continued on next page)

absence of citrate in PDH-deficient Th17 cells affects the biosynthesis of critical metabolites such as lipids.

Because lipids are essential for proliferation,[19,28] we used CellTrace Violet (CTV) to monitor the proliferation of PDH-deficient Th17 cells in culture. Although $PDH^{fl/fl}$ CD4 Cre+ Th17 cells showed significantly decreased proliferation compared with controls, proliferation was still substantial (Figure 4C), suggesting that the necessary lipids were derived from a citrate-independent source. This result prompted us to measure the uptake of extracellular lipids using fluorescently labeled palmitate (BODIPY FL C16). We observed a marked increase in uptake of this agent by the mutant cells (Figure 4D) and confirmed that ^{13}C-palmitate uptake (M16 label) was increased in PDH-deficient Th17 cells (Figure 4E). Furthermore, when cultured in medium lacking extracellular lipids, although mutant and control Th17 cells showed impaired survival and proliferation, the survival of PDH-deficient Th17 cells was more markedly impaired (Figures 4F and 4G). Moreover, lipids were essential for maintenance of the basal OCR in $PDH^{fl/fl}$ CD4 Cre+ Th17 cells (Figure 4H). These results supported our contention that the mutant cells rely on the import of extracellular lipids for proliferation and survival. However, when measuring the contribution of ^{13}C-palmitate to the generation of citrate, we detected no differences between control and PDH-deficient Th17 cells (Figure 4I). Thus, despite their increased uptake of lipids, mutant Th17 cells do not replenish the TCA cycle with carbons from lipids (Figure 4J). Taken together, these data suggest that PDH-deficient Th17 cells use extracellular fatty acids from the culture medium to directly generate the new lipids and membranes required for survival and proliferation, independent of citrate.

PDH restricts upregulation of the glutamine-mTOR-CD36 axis in Th17 cells

Long-chain fatty acids (LCFAs) require transporters such as CD36 to enter cells.[17] We observed increased CD36 expression in $PDH^{fl/fl}$ CD4 Cre+ Th17 cells, which could be partially reversed by restoring PDH expression in the mutant cells (Figures 5A and S4A). CD36 expression is controlled by mammalian target of rapamycin (mTOR),[29–31] and we detected increased phosphorylation of mTOR (p-mTOR) and its downstream target ribosomal protein S6 (p-S6) in the mutant cells (Figures 5B and 5C). CD36 induction and the observed increase in lipid uptake by PDH-deficient Th17 cells could be partially reversed by two chemical inhibitors of mTOR, Torin 1 and rapamycin (Figures 5D, 5E, S4B, and S4C).

mTOR is activated by amino acids, particularly glutamine,[32] and we had already established that PDH-deficient Th17 cells showed increased glutamine uptake and glutaminolysis (Figures 3A–3C). In line with these results, glutamine deprivation decreased p-mTOR and CD36 expression as well as lipid uptake in PDH-deficient Th17 cells to control levels (Figures 5F–5H), exposing a metabolic feedback loop regulating central carbon metabolism. Thus, it seems that PDH-deficient Th17 cells increase their mTOR activity to promote extracellular lipid uptake through CD36 and thereby maintain the survival and functionality of these cells.

PDH-derived citrate is crucial for histone acetylation and gene transcription in Th17 cells

Citrate-derived acetyl-CoA is required for post-translational histone acetylation,[19] an important epigenetic modification that opens up condensed chromatin and fosters transcriptional activity.[18] Intriguingly, when measuring total acetyl-CoA levels, we observed no differences between wild-type and PDH-deficient Th17 cells (Figure 6A). However, the contribution of ^{13}C-glucose to the acetyl-CoA pool was reduced in the mutant Th17 cells, whereas the contribution of ^{13}C-palmitate was increased (Figures 6B and 6C). Despite having normal acetyl-CoA levels, PDH-deficient Th17 cells showed reduced histone-3 lysine-27 acetylation (H3K27Ac) as well as a decrease in the contribution of glucose to the acetyl groups of histone-3 (Figures 6D, 6E, and S5A). This indicated an exclusive role of glucose-derived acetyl-CoA for histone acetylation in Th17 cells. Taken together, these data suggest that there are different pools of acetyl-CoA in Th17 cells that are derived from different carbon sources. Not all of these acetyl-CoA pools are used for histone acetylation; such a diversification has been recently documented in cancer cell lines.[33]

To analyze the effects of this decreased histone acetylation, we performed assay for transposase-accessible chromatin using sequencing (ATAC-seq) analysis[34,35] of *in vitro*-differentiated control and PDH-deficient Th17 cells. This technique revealed 39,647 significant regions with differentially opened areas in PDH-deficient Th17 cells compared with control Th17 cells with dramatically reduced open areas in the mutant cells (Figure 6F). The *Il17a*, *Il17f*, *Il23r*, *Smad3*, *Hif1a*, and *Stat3* loci showed decreases in chromatin accessibility and mRNA expression (Figures 6G and S5B). Although the accessibility of the *Rorc* locus encoding RORγT was reduced, levels of RORγT mRNA were not affected (Figure 6G), in line with the near-normal RORγT expression levels in mutant Th17 cells (Figures 1I and 1J). Similarly, the accessibility of the *Il17ra* locus was affected, whereas the mRNA levels remained unchanged (Figure S5B). Therefore, we hypothesized that the PDH-mediated synthesis

(E) GC-MS measurements of relative levels of fully labeled (M16 or M15) and unlabeled (M0) palmitate in $PDH^{fl/fl}$ and $PDH^{fl/fl}$ CD4 Cre+ Th17 cells incubated for 24 h with [U-$^{13}C_{16}$]-palmitate. Data are mean ± SEM (n = 4).
(F) Fold change in frequencies of viable $PDH^{fl/fl}$ and $PDH^{fl/fl}$ CD4 Cre+ *in vitro*-differentiated Th17 cells cultured in complete IMDM with or without lipids, gated on viable cells. Data are mean ± SEM (n = 3) and representative of 3 trials.
(G) Left: representative FCA of the proliferation of CTV-labeled $PDH^{fl/fl}$ and $PDH^{fl/fl}$ CD4 Cre+ Th17 cells cultured in complete IMDM with or without lipids. Right: fold change in division index of the Th17 cells in the left panel. Data are mean ± SEM (n = 3) and representative of 3 trials.
(H) Quantification of Seahorse determination of basal OCR in $PDH^{fl/fl}$ CD4 Cre+ *in vitro*-differentiated Th17 cells cultured in complete IMDM with or without lipids. Data are mean ± SEM (n = 3) and representative of 3 trials.
(I) MID of M0 and M2 citrate in $PDH^{fl/fl}$ and $PDH^{fl/fl}$ CD4 Cre+ Th17 cells incubated for 24 h with [U-$^{13}C_{16}$]-palmitate. Data are mean ± SEM (n = 4).
(J) Contribution to M2 citrate of labeled M15+16 palmitate in the cells in (I), expressed as a ratio. Data are mean ± SEM (n = 4).
The p values are determined by unpaired two-tailed Student's t test or one- or two-way ANOVA where appropriate. Correction for multiple comparisons was performed using the Tukey test. $^{**}p < 0.01$, $^{***}p < 0.001$, $^{****}p < 0.0001$.

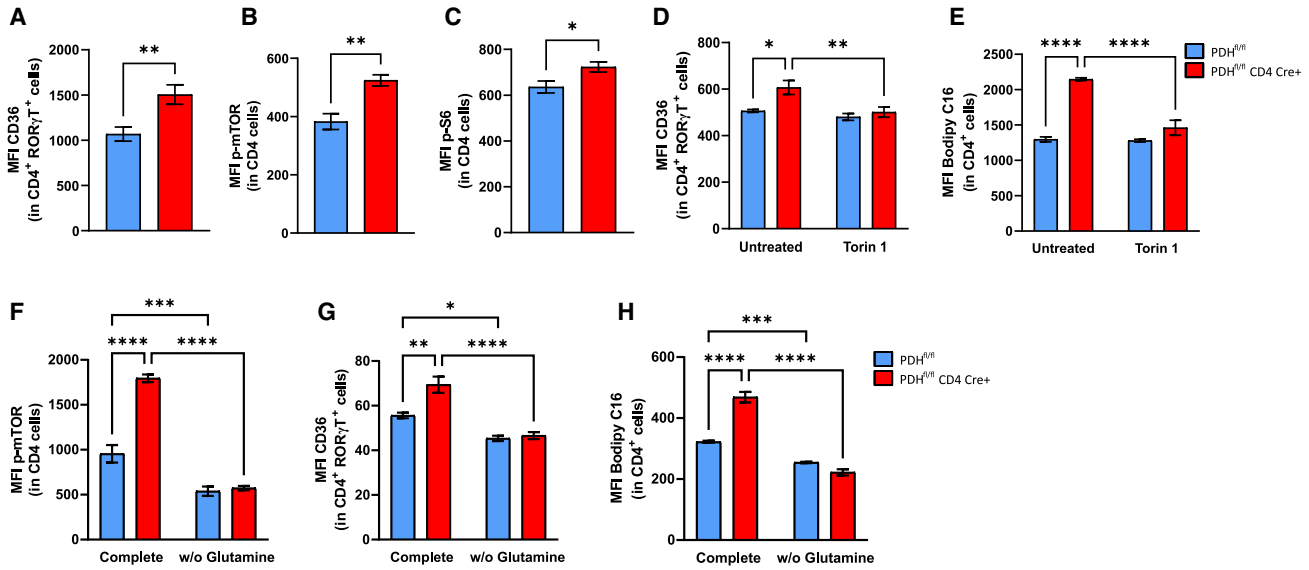

Figure 5. PDH restricts induction of the glutamine-mTOR-CD36 axis in Th17 cells

(A–C) Quantification of CD36 MFI (A), intracellular p-mTOR MFI (B), and intracellular p-S6 MFI (C) in $PDH^{fl/fl}$ and $PDH^{fl/fl}$ CD4 Cre+ Th17 cells, gated on viable $CD4^+ROR\gamma T^+$ cells. Data are mean ± SEM (n = 3) and representative of 3 trials.

(D and E) Quantification of CD36 MFI (D) and BODIPY FL C16 MFI (E) in $PDH^{fl/fl}$ and $PDH^{fl/fl}$ CD4 Cre+ *in vitro*-differentiated Th17 cells cultured with or without Torin 1 (100 nM), gated on viable $CD4^+ROR\gamma T^+$ cells. Data are mean ± SEM (n = 3) and representative of 3 trials.

(F–H) Quantification of intracellular p-mTOR MFI (F), CD36 MFI (G), and BODIPY FL C16 MFI (H) in $PDH^{fl/fl}$ and $PDH^{fl/fl}$ CD4 Cre+ *in vitro*-differentiated Th17 cells cultured in either RPMI medium containing 1% L-glutamine (complete) or RPMI medium without glutamine, gated on viable $CD4^+$ (F and H) or $CD4^+ROR\gamma T^+$ (G) cells. Data are mean ± SEM (n = 3) and representative of 2 trials.

The p values are determined by unpaired two-tailed Student's t test or two-way ANOVA where appropriate. Correction for multiple comparisons was performed using the Tukey test. *p < 0.05, **p < 0.01, ***p < 0.001, ****p < 0.0001.

of glucose-derived acetyl-CoA produces citrate that regulates Th17 cells' function via histone acetylation.

Acetate treatment restores the metabolic, epigenetic, and effector alterations caused by PDH deficiency in Th17 cells

To confirm the effects of acetylation on Th17 cells, we bypassed the PDH deficiency in $PDH^{fl/fl}$ CD4 Cre+ T cells by treating them (and control Th17 cells) with the short-chain fatty acid (SCFA) acetate,[36,37] which is converted by acetyl-CoA synthetases into acetyl-CoA.[38] Indeed, upon acetate supplementation, PDH-deficient Th17 cells increased H3K27 acetylation to wild-type levels (Figure 7A). Furthermore, to test whether acetate was incorporated into the acetyl groups on histone-3 molecules, we treated PDH-deficient and control Th17 cells with ^{13}C-labeled acetate and observed that it contributed much more intensely to histone-3 acetylation in the mutant cells (Figures 7B and S6A). Moreover, acetate treatment increased chromatin accessibility in PDH-deficient Th17 cells, as measured by ATAC-seq (Figure S6B). We also detected the contribution of ^{13}C-acetate to TCA metabolites such as citrate, fumarate, and malate in mutant Th17 cells (Figures 7C, 7D, and S6C). As expected, these contributions were increased over those in control Th17 cells because of the lack of glucose flux into the TCA cycle in the mutant cells. In addition, RNA-seq revealed that the transcriptome of acetate-treated PDH-deficient Th17 cells was similar to the transcriptomes of acetate-treated or untreated control Th17 cells (Figure 7E). Acetate treatment also restored the expression of TCA cycle enzymes to mutant Th17 cells (Figure S6D) so that the citrate pool recovered (Figure 7F). As a result, acetate-treated PDH-deficient Th17 cells were able to re-establish their *de novo* lipid synthesis, regain their proliferative potential, and normalize their basal OCR and extracellular acidification rate (ECAR) glycolysis (Figures 7G–7I and S6E). Indeed, Glut-1 expression and 2-NBDG uptake also returned to control levels in acetate-treated PDH-deficient Th17 cells (Figures 7J and 7K), as did glutamine and lipid uptake and levels of p-mTOR and CD36 (Figures 7L–7O). Finally, acetate-treated PDH-deficient Th17 cells regained the capacity to produce IL-17A (Figure 7P).

These data indicate that PDH-generated acetyl-CoA contributes to a critical citrate pool that cannot be derived from any other carbon source except exogenous acetate. This citrate pool is crucial for maintaining the correct chromatin state that allows Th17 signature gene transcription and thereby coordinates the metabolism, proliferation, and functionality of these cells.

DISCUSSION

Previous work has shown that the metabolism and functions of effector T cells are closely connected.[8,10,11,39] In our study, we genetically targeted the PDH-E1α subunit specifically in T cells, disconnecting glycolysis from the TCA cycle. Th17 cells are known to rely on glycolytic ATP and regulators such as myc, HIF-1α, and mTOR for their differentiation and function,[40–45]

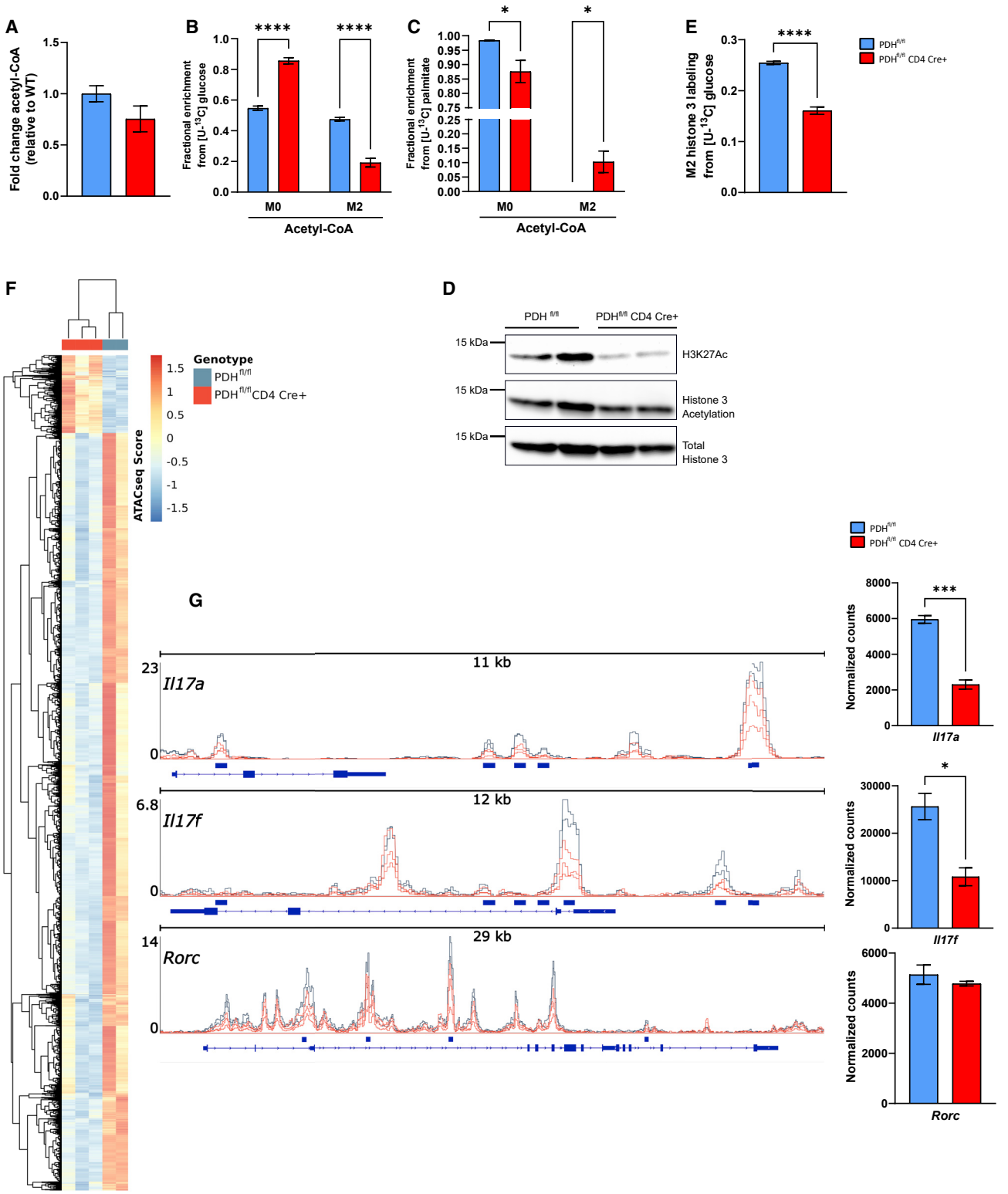

Figure 6. PDH is crucial for histone acetylation and epigenetic modifications in Th17 cells

(A) LC-MS quantification of fold change in intracellular acetyl-CoA levels in PDH$^{fl/fl}$ CD4 Cre+ Th17 cells relative to PDH$^{fl/fl}$ Th17 cells. Data are mean ± SEM (n = 3) and representative of 2 trials.

(legend continued on next page)

and we have now added PDH to this list. Without PDH, Th17 cells rewire their metabolism to increase uptake of glucose, glutamine, and fatty acids to ensure their survival and proliferation. However, our mutant Th17 cells lacked a critical citrate pool that could not be generated in a PDH-independent manner and was essential for the functionality of Th17 cells *in vivo* and *in vitro*.

The mitochondrial pyruvate carrier (MPC) imports pyruvate into the mitochondria, where it is converted into acetyl-CoA.[46–48] MPC1$^{fl/fl}$ Vav Cre mutant mice, which do not express *Mpc1* in any hematopoietic cells, suffer from more severe EAE than control littermates,[49] a finding that contrasts with the effects of T cell-specific PDH deletion we observed. However, pyruvate in the mitochondria can also be generated from glutamine in Th17 cells, as shown previously,[50] which could provide a substrate for PDH while bypassing the need for MPC-mediated pyruvate import. We surmise that PDH-dependent conversion of pyruvate to acetyl-CoA, and not its transport into the mitochondria, might be essential for Th17 cell effector function during EAE. In another study, Wenes et al.[51] showed that MPC deletion in CD8$^+$ T cells induced increased uptake of fatty acids and glutamine, similar to our findings. However, in this context, acetyl-CoA production was induced in the mutant cells.[51] As a result, histone acetylation of genes supporting memory T cell development was increased, promoting CD8$^+$ memory T cell differentiation. In addition, a different study showed that PDH could be localized in the nucleus in a constitutively active form.[52] The generation of acetyl-CoA in the nucleus could explain the discrepancies between the Ramstead et al.[49] article and our data because PDH is deleted in both, mitochondria and nucleus, in our study, while MPC is only expressed in the mitochondria. These results stand in clear contrast to our findings but strengthen our theory that a PDH-dependent acetyl-CoA pool is necessary for histone acetylation.

It is also possible that the developmental stage at which pyruvate metabolism is disrupted defines its effects. VavCre-mediated MPC1 deletion occurs very early during hematopoiesis and so affects T cell development, which favors the establishment of a more activated T cell pool.[49] Similarly, when Mx1Cre is employed to delete PDH in bone marrow and hematopoietic stem cells, T cell development in the thymus is impaired, which is not the case when CD4 Cre is used.[53] However, it was surprising that, during EAE progression, we found decreased amounts of Treg cells in the brains of mice bearing PDH-deficient T cells, whereas the differentiation of this cell subset *in vitro* was not affected. This result is puzzling because it has been shown previously that Treg cells rely heavily on mitochondrial oxidation for their suppressive abilities.[9] These data suggest that how PDH operates during T cell development, and PDH's effects on Treg function, are worthy of further investigation.

Tight regulation of metabolism is important for maintaining Th cell functionality,[54] and too much or too little glycolysis and/or OXPHOS impairs T cell functions.[55,56] Our data show that abrogation of PDH activity affects Th17 cell functionality. Conversely, sustained PDH activation achieved by pharmacological inhibition of PDK1 (an inhibitor of PDH) also has a negative effect on Th17 cells.[57] Thus, PDH is a vital regulator of Th17 cell functions, consistent with the idea that too little or too much flux through this metabolic gatekeeper is detrimental to Th17 cells.

Glutamine contributes to the energy produced via the TCA cycle,[27] and ablation of glutaminase impairs Th17 cell differentiation and function so that Th17-driven inflammatory diseases are mitigated *in vivo*.[50] Glutamine is also required for the synthesis of glutathione (GSH), an important antioxidant in T cells that is essential for effector T cell reprogramming and Treg cell suppressive capacity.[55,56] However, we showed that increased glutamine uptake did not relieve the functional defects of PDH-deficient Th17 cells because glutamine could not replenish the critical PDH-dependent citrate pool in these cells. Thus, only stringent control of a specific metabolic program in a given Th subset can ensure cell functionality. Fortunately, this restriction offers the possibility of subset-specific therapeutic interference at key regulatory points.

Upon PDH deletion, Th17 cells were unable to generate fatty acids *de novo*. Instead, they increased their uptake of extracellular fatty acids through mTOR-dependent upregulation of CD36. Although CD36 is a target of mTOR signaling, mTOR is also crucial for Th17 cell differentiation and metabolic rewiring.[58–60] A major activator of mTOR is glutamine,[32] and the increased mTOR activation in our PDH-deficient Th17 cells was causally linked to their heightened glutamine uptake. These data reveal a metabolic feedback loop between glycolysis and glutaminolysis in Th17 cells that can respond to exogenous acetyl-CoA in the form of acetate. Acetate treatment of PDH-deficient Th17 cells reversed the metabolic dysregulation in these cells and restored their functionality. Similarly, other studies have shown that acetate can serve as a source of acetyl-CoA to regulate effector T cell functions.[37,45,61] These

(B and C) MID of M0 and M2 acetyl-CoA in PDH$^{fl/fl}$ and PDH$^{fl/fl}$ CD4 Cre+ Th17 cells incubated for 24 h with [U-$^{13}C_5$]-glucose (B) or [U-$^{13}C_{16}$]-palmitate (C). Data are mean ± SEM (n = 3) and representative of 2 trials.

(D) Representative immunoblot to detect histone-3 lysine-27 acetylation (H3K27Ac) and histone-3 acetylation in Th17 cells from two PDH$^{fl/fl}$ and two PDH$^{fl/fl}$ CD4 Cre+ mice. Total histone-3, loading control. Data are representative of 3 mice/genotype.

(E) MID of M2 histone-3 labeling in PDH$^{fl/fl}$ and PDH$^{fl/fl}$ CD4 Cre+ Th17 cells incubated for 24 h with [U-$^{13}C_5$]-glucose. Data are mean ± SEM (n = 4) and representative of 2 trials.

(F) Heatmap of ATAC-seq showing significantly differentially accessible regions (DBSs) in PDH$^{fl/fl}$ vs. PDH$^{fl/fl}$ CD4 Cre+ Th17 cells as identified by DiffBind. The ATAC-seq score is the *Z* score for the normalized count of each DBS.

(G) Left: plot of chromatin accessibility at the *Il17a*, *Il17f*, and *Rorc* loci in PDH$^{fl/fl}$ (blue lines) and PDH$^{fl/fl}$ CD4 Cre+ (red lines) Th17 cells. Dark blue bars depict significant DBSs as identified by DiffBind. Above each ATAC trace, a scale bar indicates the size of the genomics sequence covered in the graph. For each gene, the local sequence coverage observed in the ATAC experiment is shown as normalized counts (left x axis) obtained by scaling to normalization factors observed with DiffBind. Right: quantitation of *Il17a*, *Il17f*, and *Rorc* mRNA levels (normalized counts) in PDH$^{fl/fl}$ and PDH$^{fl/fl}$ CD4 Cre+ Th17 cells as measured by RNA-seq. The p values are determined by unpaired two-tailed Student's t test or two-way ANOVA where appropriate. Correction for multiple comparisons was performed using the Tukey test. *p < 0.05, ***p < 0.001, ****p < 0.0001.

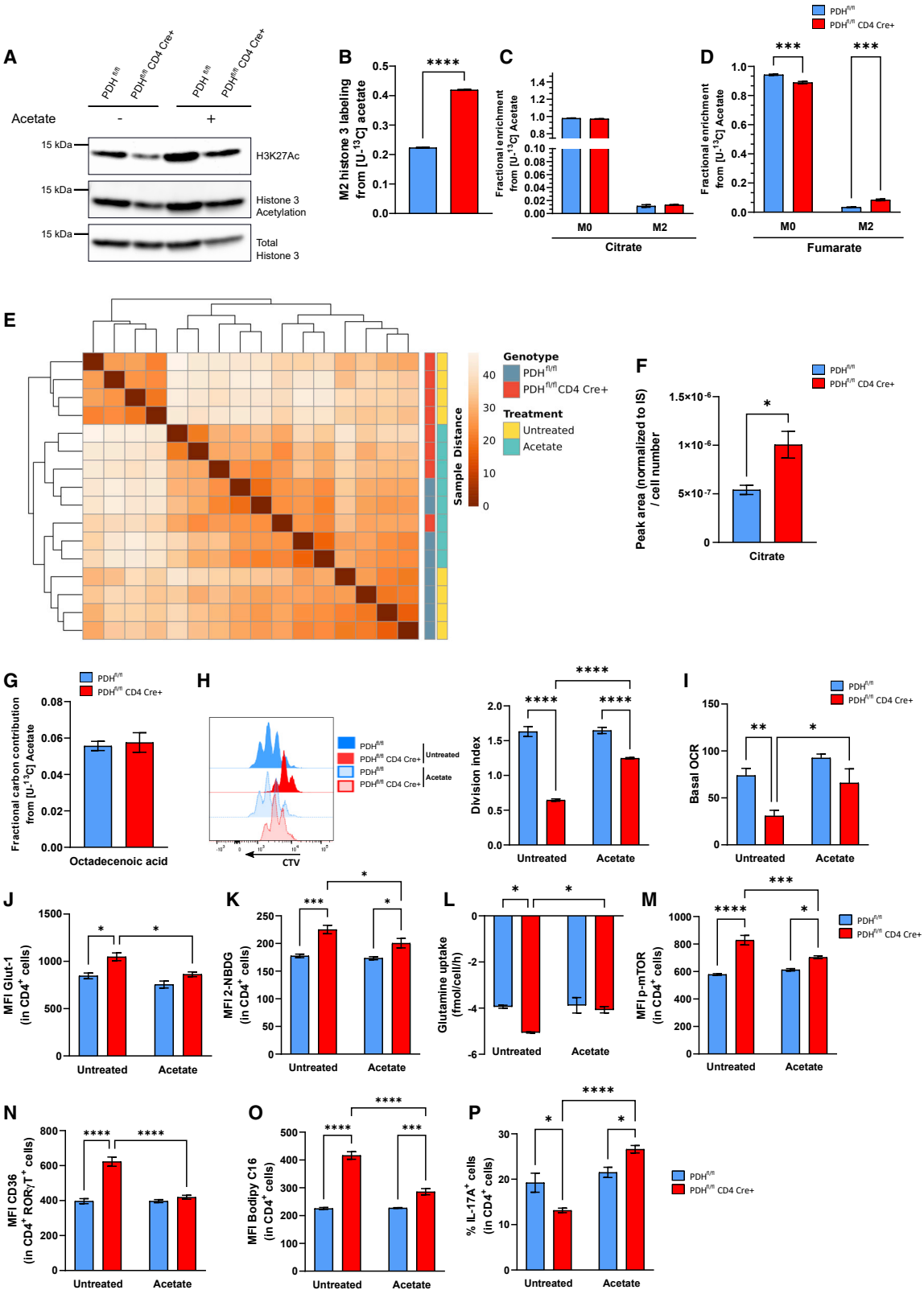

(legend on next page)

aspects of cellular metabolism are closely linked to epigenetic modifications. However, in contrast to our findings, Peng et al.[61] showed that LDH ablation in Th1 cells leads to reduced acetyl-CoA levels and, thus, histone acetylation, impairing IFNγ production. We demonstrated that our PDH-deficient T cells are perfectly capable of Th1 cell differentiation and IFNγ production. This discrepancy could be due to the fact that Th17 cells rely on glucose-derived acetyl-CoA for histone acetylation, whereas Th1 cells are able to use other acetyl-CoA pools for that purpose. When PDH localizes in the nucleus in a constitutively active form, it generates a mitochondrion-independent pool of acetyl-CoA for histone acetylation.[52] We demonstrated that an absence of PDH impairs histone H3K27Ac in a manner that can be restored by acetate treatment, emphasizing the importance of PDH for maintaining normal epigenetic control in Th17 cells. However, we would like to mention that chromatin accessibility can be regulated by non-classical histone modifications that are distinct from acetylation.[62]

Our results are bolstered by a recent study showing that ablation of Glut-3 in murine T cells also impairs Th17 effector function.[63] These mutant mice were protected against developing EAE because Glut-3-derived acetyl-CoA production and epigenetic modifications were defective. Our study highlights the importance of regulating metabolism and defining the connections between metabolic disruptions and epigenetic modulations in Th17 cells.

In conclusion, our study uncovered an unexpected role of PDH as a central regulator of the effector functions of Th17 cells *in vivo* and *in vitro*. In particular, Th17 cells use PDH for establishment of a glucose-derived citrate pool that controls the chromatin accessibility of Th17-specific loci and, thus, the survival, proliferation, and effector functions of these cells. Furthermore, this work uncovered potential targets for the therapy of Th17 cell-driven autoimmune diseases.

Limitations of the study

(1) Our study deciphers the role of the catalytic subunit of PDH in Th17 cell differentiation and function in mice *in vitro* and *in vivo*. While we show an impact during EAE, a mouse model of multiple sclerosis, the role of PDH in human subjects of this particular subset and Th17 cell-driven diseases was not analyzed. (2) This study uses cells harboring a T cell-specific deletion of the catalytic subunit of PDH and focuses on its function (i.e., conversion of pyruvate into acetyl-CoA). However, we cannot exclude potential structural effects of ablation of PDH E1α that might contribute to our results. (3) Here, we focus on the role of a glucose-derived pool of citrate and its importance in Th17 cell function. However, we describe that there are no significant differences in cellular acetyl-CoA concentrations between control and PDH-deficient Th17 cells. This points to an alternative source and an alternative acetyl-CoA pool with distinct functionality, which we have not been able to identify in this study.

STAR★METHODS

Detailed methods are provided in the online version of this paper and include the following:

- KEY RESOURCES TABLE
- RESOURCE AVAILABILITY
  - Lead contact
  - Materials availability
  - Data and code availability
- EXPERIMENTAL MODEL AND SUBJECT DETAILS
  - Mice

Figure 7. Acetate treatment reverses the effects caused by PDH ablation in Th17 cells

(A) Representative immunoblot to detect H3K27Ac and histone-3 acetylation in $PDH^{fl/fl}$ and $PDH^{fl/fl}$ CD4 Cre+ Th17 cells treated with (+) or without (−) acetate (10 mM). Total histone-3, loading control. Data are representative of 3 mice/genotype.

(B) MID of M2 histone-3 labeling in $PDH^{fl/fl}$ and $PDH^{fl/fl}$ CD4 Cre+ Th17 cells incubated for 72 h with [U-$^{13}C_2$]-acetate. Data are mean ± SEM (n = 4) and representative of 2 trials.

(C and D) MID of M0 and M2 citrate (C) and M0 and M2 fumarate (D) in $PDH^{fl/fl}$ and $PDH^{fl/fl}$ CD4 Cre+ Th17 cells incubated for 72 h with [U-$^{13}C_2$]-acetate. Data are mean ± SEM (n = 3) and representative of 2 trials.

(E) Sample distance matrix between the RNA-seq normalized counts of $PDH^{fl/fl}$ and $PDH^{fl/fl}$ CD4 Cre+ Th17 cells cultured in complete IMDM and treated or not with acetate (10 mM). Results shown are after conversion to homoskedastic data by variance stabilizing transformation.

(F) Quantification of intracellular citrate in $PDH^{fl/fl}$ and $PDH^{fl/fl}$ CD4 Cre+ Th17 cells incubated for 72 h with acetate (10 mM). Data are mean ± SEM (n = 3) and representative of 2 trials.

(G) Fractional carbon contribution of ^{13}C-acetate to octadecenoic acid in $PDH^{fl/fl}$ and $PDH^{fl/fl}$ CD4 Cre+ Th17 cells. Data are mean ± SEM (n = 3) and representative of 2 trials.

(H) Left: representative FCA of the proliferation of CTV-labeled $PDH^{fl/fl}$ and $PDH^{fl/fl}$ CD4 Cre+ Th17 cells cultured in complete IMDM and treated or not with acetate (10 mM). Right: division index of the Th17 cells in the left panel. Data are mean ± SEM (n = 3) and representative of 3 trials.

(I) Quantification of Seahorse determination of basal OCR in $PDH^{fl/fl}$ and $PDH^{fl/fl}$ CD4 Cre+ *in vitro*-differentiated Th17 cells treated or not with acetate (10 mM). Data are mean ± SEM (n = 3) and representative of 3 trials.

(J and K) Quantification of Glut-1 MFI (J) and 2-NBDG MFI (K) in $PDH^{fl/fl}$ and $PDH^{fl/fl}$ CD4 Cre+ *in vitro*-differentiated Th17 cells treated or not with acetate (10 mM), gated on viable $CD4^+$ cells. Data are mean ± SEM (n = 3) and representative of 3 trials.

(L) YSI quantification of glutamine uptake from the culture medium of $PDH^{fl/fl}$ and $PDH^{fl/fl}$CD4 Cre+ Th17 cells treated or not with acetate (10 mM). Data are mean ± SEM (n = 3) and representative of 2 trials.

(M–O) Quantification of intracellular p-mTOR MFI (M), CD36 MFI (N), and BODIPY FL C16 MFI (O) in $PDH^{fl/fl}$ and $PDH^{fl/fl}$ CD4 Cre+ *in vitro*-differentiated Th17 cells treated or not with acetate (10 mM), gated on viable $CD4^+$ cells. Data are mean ± SEM (n = 3) and representative of 3 trials.

(P) Intracellular FCA of frequencies of IL-$17A^+$ cells among $PDH^{fl/fl}$ and $PDH^{fl/fl}$ CD4 Cre+ Th17 cells treated or not with acetate (10 mM) and stimulated for 5 h with PMA/Iono, gated on viable $CD4^+$ cells. Data are mean ± SEM (n = 3) and representative of 4 trials.

The p values are determined by unpaired two-tailed Student's t test or two-way ANOVA where appropriate. Correction for multiple comparisons was performed using the Tukey test. *p < 0.05, **p < 0.01, ***p < 0.001, ****p < 0.0001.

SUPPLEMENTAL INFORMATION

Supplemental information can be found online at https://doi.org/10.1016/j.celrep.2023.112153.

ACKNOWLEDGMENTS

We are grateful to Max Löhning (Charité University Berlin) and Alexander Skupin (University of Luxembourg) for helpful discussions, Dr. Aurelien Ginolhac (University of Luxembourg) for bioinformatic analysis, the Metabolomics Platform of the Luxembourg Center for Systems Biomedicine (LCSB; University of Luxembourg) for metabolomics data, Dr. Rashi Halder of the Sequencing Platform of the LCSB for sequencing data (RRID: SCR_021931), the High-Performance Computing (HPC) platform (University of Luxembourg), and the National Cytometry Platform (LIH; Luxembourg) for support with flow cytometry. We also thank Samantha Storn, Anaïs Oudin, all Animal Facility staff, and LIH's Animal Welfare Structure for animal services at LIH, Luxembourg, and Djalil Coowar, Jennifer Behm, Marthe Schmit and all Animal Facility staff for animal services at the University of Luxembourg.

D.B. is supported by FNR-ATTRACT (A14/BM/7632103) and FNR-CORE grants (C21/BM/15796788 and C18/BM/12691266). D.B., T.K., and C.D. are supported by FNRS-Televie grants 7.4587.20 and/or 7.497.19; D.B., L.B., L.G., and L.S.-B. by FNR-PRIDE (PRIDE/11012546/NEXTIMMUNE); D.B. and A.E. by PRIDE17/11823097/MicrOH; D.B. and D.G.F. by FNR-RIKEN (TregBar/11228353); S.H. by FNR-PRIDE (PRIDE17/12244779/PARK-Q); D.G. by a postdoctoral fellowship from the Fondation du Pélican de Mie et Pierre Hippert-Faber; J.M. by FNR-ATTRACT (A18/BM/11809970); and M.M. by FNR PEARL (P16/BM/11192868).

AUTHOR CONTRIBUTIONS

L.S.-B. performed most experiments, assisted by M.G., H.K., L.B., A.E., L.G., D.G.F., C.B., C.V., and S.F. L.S.-B., M.G., and C.B. isolated brains and spleens from EAE mice. L.S.-B., H.K., A.E., and D.G.F. performed Seahorse flux assays. Isotopic and metabolic tracing experiments were performed by L.S.-B., M.G., and H.K. and analyzed by M.B. and J.M. Histone and palmitate tracing experiments were performed and analyzed by T.H.M. and A.H. Analysis of RNA-seq data was performed by J.L. and S.H. ATAC-seq and data analysis were performed by S.H., D.G., and L.S. T.K., C.D., J.-J.G., C.J., M.M., L.S., K.H., and J.M. provided reagents and expert comments. D.B. supervised the project. L.S.-B. and D.B. conceptualized the work, designed all experiments, analyzed data, and wrote the manuscript. All authors reviewed and edited the final manuscript.

DECLARATION OF INTERESTS

The authors declare no competing interests.

INCLUSION AND DIVERSITY

We support inclusive, diverse, and equitable conduct of research.

Received: April 5, 2022
Revised: December 5, 2022
Accepted: February 7, 2023
Published: February 26, 2023

REFERENCES

1. Pearce, E.L., Poffenberger, M.C., Chang, C.-H., and Jones, R.G. (2013). Fueling immunity: insights into metabolism and lymphocyte function. Science *342*, 1242454. https://doi.org/10.1126/science.1242454.
2. Aranami, T., and Yamamura, T. (2008). Th17 cells and autoimmune encephalomyelitis (EAE/MS). Allergol. Int. *57*, 115–120. https://doi.org/10.2332/allergolint.R-07-159.
3. Basu, R., Hatton, R.D., and Weaver, C.T. (2013). The Th17 family: flexibility follows function. Immunol. Rev. *252*, 89–103. https://doi.org/10.1111/imr.12035.
4. Wu, B., and Wan, Y. (2020). Molecular control of pathogenic Th17 cells in autoimmune diseases. Int. Immunopharm. *80*, 106187. https://doi.org/10.1016/j.intimp.2020.106187.
5. Franchina, D.G., Dostert, C., and Brenner, D. (2018). Reactive oxygen species: involvement in T cell signaling and metabolism. Trends Immunol. *39*, 489–502. https://doi.org/10.1016/j.it.2018.01.005.
6. Guerra, L., Bonetti, L., and Brenner, D. (2020). Metabolic modulation of immunity: a new concept in cancer immunotherapy. Cell Rep. *32*, 107848. https://doi.org/10.1016/j.celrep.2020.107848.
7. Pearce, E.L., and Pearce, E.J. (2013). Metabolic pathways in immune cell activation and quiescence. Immunity *38*, 633–643. https://doi.org/10.1016/j.immuni.2013.04.005.
8. Buck, M.D., O'Sullivan, D., and Pearce, E.L. (2015). T cell metabolism drives immunity. J. Exp. Med. *212*, 1345–1360. https://doi.org/10.1084/jem.20151159.
9. Kurniawan, H., Soriano-Baguet, L., and Brenner, D. (2020). Regulatory T cell metabolism at the intersection between autoimmune diseases and cancer. Eur. J. Immunol. *50*, 1626–1642. https://doi.org/10.1002/eji.201948470.
10. Rangel Rivera, G.O., Knochelmann, H.M., Dwyer, C.J., Smith, A.S., Wyatt, M.M., Rivera-Reyes, A.M., Thaxton, J.E., and Paulos, C.M. (2021). Fundamentals of T Cell metabolism and strategies to enhance cancer immunotherapy. Front. Immunol. *12*, 645242. https://doi.org/10.3389/fimmu.2021.645242.
11. Chapman, N.M., and Chi, H. (2022). Metabolic adaptation of lymphocytes in immunity and disease. Immunity *55*, 14–30. https://doi.org/10.1016/j.immuni.2021.12.012.
12. DeBrosse, S.D., and Kerr, D.S. (2016). Pyruvate dehydrogenase complex deficiency. In Mitochondrial Case Studies (Elsevier), pp. 93–101. https://doi.org/10.1016/B978-0-12-800877-5.00012-7.
13. O'Neill, L.A.J., Kishton, R.J., and Rathmell, J. (2016). A guide to immunometabolism for immunologists. Nat. Rev. Immunol. *16*, 553–565. https://doi.org/10.1038/nri.2016.70.

14. Wellen, K.E., Hatzivassiliou, G., Sachdeva, U.M., Bui, T.V., Cross, J.R., and Thompson, C.B. (2009). ATP-citrate lyase links cellular metabolism to histone acetylation. Science *324*, 1076–1080. https://doi.org/10.1126/science.1164097.

15. Wang, R., and Green, D.R. (2012). Metabolic reprogramming and metabolic dependency in T cells. Immunol. Rev. *249*, 14–26. https://doi.org/10.1111/j.1600-065X.2012.01155.x.

16. Zhao, S., Torres, A., Henry, R.A., Trefely, S., Wallace, M., Lee, J.V., Carrer, A., Sengupta, A., Campbell, S.L., Kuo, Y.-M., et al. (2016). ATP-citrate lyase controls a glucose-to-acetate metabolic switch. Cell Rep. *17*, 1037–1052. https://doi.org/10.1016/j.celrep.2016.09.069.

17. Koundouros, N., and Poulogiannis, G. (2020). Reprogramming of fatty acid metabolism in cancer. Br. J. Cancer *122*, 4–22. https://doi.org/10.1038/s41416-019-0650-z.

18. Li, B., Carey, M., and Workman, J.L. (2007). The role of chromatin during transcription. Cell *128*, 707–719. https://doi.org/10.1016/j.cell.2007.01.015.

19. Pietrocola, F., Galluzzi, L., Bravo-San Pedro, J.M., Madeo, F., and Kroemer, G. (2015). Acetyl coenzyme A: a central metabolite and second messenger. Cell Metabol. *21*, 805–821. https://doi.org/10.1016/j.cmet.2015.05.014.

20. Sivanand, S., Viney, I., and Wellen, K.E. (2018). Spatiotemporal control of acetyl-CoA metabolism in chromatin regulation. Trends Biochem. Sci. *43*, 61–74. https://doi.org/10.1016/j.tibs.2017.11.004.

21. Yang, W., Pang, D., Chen, M., Du, C., Jia, L., Wang, L., He, Y., Jiang, W., Luo, L., Yu, Z., et al. (2021). Rheb mediates neuronal-activity-induced mitochondrial energetics through mTORC1-independent PDH activation. Dev. Cell *56*, 811–825.e6. https://doi.org/10.1016/j.devcel.2021.02.022.

22. Baricza, E., Marton, N., Királyhidi, P., Kovács, O.T., Kovácsné Székely, I., Lajkó, E., Kőhidai, L., Rojkovich, B., Érsek, B., Buzás, E.I., and Nagy, G. (2018). Distinct in vitro T-helper 17 differentiation capacity of peripheral naive T cells in rheumatoid and psoriatic arthritis. Front. Immunol. *9*, 606. https://doi.org/10.3389/fimmu.2018.00606.

23. Macintyre, A.N., Gerriets, V.A., Nichols, A.G., Michalek, R.D., Rudolph, M.C., Deoliveira, D., Anderson, S.M., Abel, E.D., Chen, B.J., Hale, L.P., and Rathmell, J.C. (2014). The glucose transporter Glut1 is selectively essential for CD4 T cell activation and effector function. Cell Metabol. *20*, 61–72. https://doi.org/10.1016/j.cmet.2014.05.004.

24. Zou, C., Wang, Y., and Shen, Z. (2005). 2-NBDG as a fluorescent indicator for direct glucose uptake measurement. J. Biochem. Biophys. Methods *64*, 207–215. https://doi.org/10.1016/j.jbbm.2005.08.001.

25. Katsen, M., Soderman, D., and Nitowsky, M. (1965). Kinetic and electrophoretic evidence for multiple forms of glucose-ATP phosphotransferase activity from human cell cultures and rat liver. Biochem. Biophys. Res. Commun. *19*, 6.

26. Buescher, J.M., Antoniewicz, M.R., Boros, L.G., Burgess, S.C., Brunengraber, H., Clish, C.B., DeBerardinis, R.J., Feron, O., Frezza, C., Ghesquiere, B., et al. (2015). A roadmap for interpreting 13 C metabolite labeling patterns from cells. Curr. Opin. Biotechnol. *34*, 189–201. https://doi.org/10.1016/j.copbio.2015.02.003.

27. Yoo, H.C., Yu, Y.C., Sung, Y., and Han, J.M. (2020). Glutamine reliance in cell metabolism. Exp. Mol. Med. *52*, 1496–1516. https://doi.org/10.1038/s12276-020-00504-8.

28. de Jong, A.J., Kloppenburg, M., Toes, R.E.M., and Ioan-Facsinay, A. (2014). Fatty acids, lipid mediators, and T-cell function. Front. Immunol. *5*, 483. https://doi.org/10.3389/fimmu.2014.00483.

29. Wang, C., Yan, Y., Hu, L., Zhao, L., Yang, P., Moorhead, J.F., Varghese, Z., Chen, Y., and Ruan, X.Z. (2014). Rapamycin-mediated CD36 translational suppression contributes to alleviation of hepatic steatosis. Biochem. Biophys. Res. Commun. *447*, 57–63. https://doi.org/10.1016/j.bbrc.2014.03.103.

30. Angela, M., Endo, Y., Asou, H.K., Yamamoto, T., Tumes, D.J., Tokuyama, H., Yokote, K., and Nakayama, T. (2016). Fatty acid metabolic reprogramming via mTOR-mediated inductions of PPARγ directs early activation of T cells. Nat. Commun. *7*, 13683. https://doi.org/10.1038/ncomms13683.

31. Wipperman, M.F., Montrose, D.C., Gotto, A.M., and Hajjar, D.P. (2019). Mammalian target of rapamycin. Am. J. Pathol. *189*, 492–501. https://doi.org/10.1016/j.ajpath.2018.11.013.

32. Takahara, T., Amemiya, Y., Sugiyama, R., Maki, M., and Shibata, H. (2020). Amino acid-dependent control of mTORC1 signaling: a variety of regulatory modes. J. Biomed. Sci. *27*, 87. https://doi.org/10.1186/s12929-020-00679-2.

33. Izzo, L., Trefely, S., Demetriadou, C., Drummond, J., Mizukami, T., Kuprasertkul, N., Farria, A., Nguyen, P., Reich, L., Shaffer, J., et al. (2022). The carnitine shuttle links mitochondrial metabolism to histone acetylation and lipogenesis. Cell Biol. https://doi.org/10.1101/2022.09.24.509197.

34. Buenrostro, J.D., Giresi, P.G., Zaba, L.C., Chang, H.Y., and Greenleaf, W.J. (2013). Transposition of native chromatin for fast and sensitive epigenomic profiling of open chromatin, DNA-binding proteins and nucleosome position. Nat. Methods *10*, 1213–1218. https://doi.org/10.1038/nmeth.2688.

35. Buenrostro, J.D., Wu, B., Chang, H.Y., and Greenleaf, W.J. (2015). ATAC-seq: a method for assaying chromatin accessibility genome-wide. Curr. Protoc. Mol. Biol. *109*, 21.29.1–21.29.9. https://doi.org/10.1002/0471142727.mb2129s109.

36. Bulusu, V., Tumanov, S., Michalopoulou, E., van den Broek, N.J., MacKay, G., Nixon, C., Dhayade, S., Schug, Z.T., Vande Voorde, J., Blyth, K., et al. (2017). Acetate recapturing by nuclear acetyl-CoA synthetase 2 prevents loss of histone acetylation during oxygen and serum limitation. Cell Rep. *18*, 647–658. https://doi.org/10.1016/j.celrep.2016.12.055.

37. Qiu, J., Villa, M., Sanin, D.E., Buck, M.D., O'Sullivan, D., Ching, R., Matsushita, M., Grzes, K.M., Winkler, F., Chang, C.-H., et al. (2019). Acetate promotes T cell effector function during glucose restriction. Cell Rep. *27*, 2063–2074.e5. https://doi.org/10.1016/j.celrep.2019.04.022.

38. Comerford, S.A., Huang, Z., Du, X., Wang, Y., Cai, L., Witkiewicz, A.K., Walters, H., Tantawy, M.N., Fu, A., Manning, H.C., et al. (2014). Acetate dependence of tumors. Cell *159*, 1591–1602. https://doi.org/10.1016/j.cell.2014.11.020.

39. Chapman, N.M., Boothby, M.R., and Chi, H. (2020). Metabolic coordination of T cell quiescence and activation. Nat. Rev. Immunol. *20*, 55–70. https://doi.org/10.1038/s41577-019-0203-y.

40. Dang, E.V., Barbi, J., Yang, H.-Y., Jinasena, D., Yu, H., Zheng, Y., Bordman, Z., Fu, J., Kim, Y., Yen, H.-R., et al. (2011). Control of TH17/treg balance by hypoxia-inducible factor 1. Cell *146*, 772–784. https://doi.org/10.1016/j.cell.2011.07.033.

41. Michalek, R.D., Gerriets, V.A., Jacobs, S.R., Macintyre, A.N., MacIver, N.J., Mason, E.F., Sullivan, S.A., Nichols, A.G., and Rathmell, J.C. (2011). Cutting edge: distinct glycolytic and lipid oxidative metabolic programs are essential for effector and regulatory CD4 $^{+}$ T cell subsets. J. Immunol. *186*, 3299–3303. https://doi.org/10.4049/jimmunol.1003613.

42. Shi, L.Z., Wang, R., Huang, G., Vogel, P., Neale, G., Green, D.R., and Chi, H. (2011). HIF1α–dependent glycolytic pathway orchestrates a metabolic checkpoint for the differentiation of TH17 and Treg cells. J. Exp. Med. *208*, 1367–1376. https://doi.org/10.1084/jem.20110278.

43. Wang, R., Dillon, C.P., Shi, L.Z., Milasta, S., Carter, R., Finkelstein, D., McCormick, L.L., Fitzgerald, P., Chi, H., Munger, J., and Green, D.R. (2011). The transcription factor myc controls metabolic reprogramming upon T lymphocyte activation. Immunity *35*, 871–882. https://doi.org/10.1016/j.immuni.2011.09.021.

44. Zhang, D., Jin, W., Wu, R., Li, J., Park, S.-A., Tu, E., Zanvit, P., Xu, J., Liu, O., Cain, A., and Chen, W. (2019). High glucose intake exacerbates autoimmunity through reactive-oxygen-species-mediated TGF-β cytokine activation. Immunity *51*, 671–681.e5. https://doi.org/10.1016/j.immuni.2019.08.001.

45. Xu, K., Yin, N., Peng, M., Stamatiades, E.G., Chhangawala, S., Shyu, A., Li, P., Zhang, X., Do, M.H., Capistrano, K.J., et al. (2021). Glycolytic ATP fuels phosphoinositide 3-kinase signaling to support effector T helper 17 cell

responses. Immunity *54*, 976–987.e7. https://doi.org/10.1016/j.immuni.2021.04.008.

46. Bricker, D.K., Taylor, E.B., Schell, J.C., Orsak, T., Boutron, A., Chen, Y.-C., Cox, J.E., Cardon, C.M., Van Vranken, J.G., Dephoure, N., et al. (2012). A mitochondrial pyruvate carrier required for pyruvate uptake in yeast, *Drosophila* , and humans. Science *337*, 96–100. https://doi.org/10.1126/science.1218099.
47. Herzig, S., Raemy, E., Montessuit, S., Veuthey, J.-L., Zamboni, N., Westermann, B., Kunji, E.R.S., and Martinou, J.-C. (2012). Identification and functional expression of the mitochondrial pyruvate carrier. Science *337*, 93–96. https://doi.org/10.1126/science.1218530.
48. Zangari, J., Petrelli, F., Maillot, B., and Martinou, J.-C. (2020). The multifaceted pyruvate metabolism: role of the mitochondrial pyruvate carrier. Biomolecules *10*, 1068. https://doi.org/10.3390/biom10071068.
49. Ramstead, A.G., Wallace, J.A., Lee, S.-H., Bauer, K.M., Tang, W.W., Ekiz, H.A., Lane, T.E., Cluntun, A.A., Bettini, M.L., Round, J.L., et al. (2020). Mitochondrial pyruvate carrier 1 promotes peripheral T cell homeostasis through metabolic regulation of thymic development. Cell Rep. *30*, 2889–2899.e6. https://doi.org/10.1016/j.celrep.2020.02.042.
50. Johnson, M.O., Wolf, M.M., Madden, M.Z., Andrejeva, G., Sugiura, A., Contreras, D.C., Maseda, D., Liberti, M.V., Paz, K., Kishton, R.J., et al. (2018). Distinct regulation of Th17 and Th1 cell differentiation by glutaminase-dependent metabolism. Cell *175*, 1780–1795.e19. https://doi.org/10.1016/j.cell.2018.10.001.
51. Wenes, M., Jaccard, A., Wyss, T., Maldonado-Pérez, N., Teoh, S.T., Lepez, A., Renaud, F., Franco, F., Waridel, P., Yacoub Maroun, C., et al. (2022). The mitochondrial pyruvate carrier regulates memory T cell differentiation and antitumor function. Cell Metabol. *34*, 731–746.e9. https://doi.org/10.1016/j.cmet.2022.03.013.
52. Sutendra, G., Kinnaird, A., Dromparis, P., Paulin, R., Stenson, T.H., Haromy, A., Hashimoto, K., Zhang, N., Flaim, E., and Michelakis, E.D. (2014). A nuclear pyruvate dehydrogenase complex is important for the generation of acetyl-CoA and histone acetylation. Cell *158*, 84–97. https://doi.org/10.1016/j.cell.2014.04.046.
53. Jun, S., Mahesula, S., Mathews, T.P., Martin-Sandoval, M.S., Zhao, Z., Piskounova, E., and Agathocleous, M. (2021). The requirement for pyruvate dehydrogenase in leukemogenesis depends on cell lineage. Cell Metabol. *33*, 1777–1792.e8. https://doi.org/10.1016/j.cmet.2021.07.016.
54. Marelli-Berg, F.M., Fu, H., and Mauro, C. (2012). Molecular mechanisms of metabolic reprogramming in proliferating cells: implications for T-cell-mediated immunity: the metabolic control of T-cell immunity. Immunology *136*, 363–369. https://doi.org/10.1111/j.1365-2567.2012.03583.x.
55. Mak, T.W., Grusdat, M., Duncan, G.S., Dostert, C., Nonnenmacher, Y., Cox, M., Binsfeld, C., Hao, Z., Brüstle, A., Itsumi, M., et al. (2017). Glutathione primes T cell metabolism for inflammation. Immunity *46*, 675–689. https://doi.org/10.1016/j.immuni.2017.03.019.
56. Kurniawan, H., Franchina, D.G., Guerra, L., Bonetti, L., - Baguet, L.S., Grusdat, M., Schlicker, L., Hunewald, O., Dostert, C., Merz, M.P., et al. (2020). Glutathione restricts serine metabolism to preserve regulatory T cell function. Cell Metabol. *31*, 920–936.e7. https://doi.org/10.1016/j.cmet.2020.03.004.
57. Gerriets, V.A., Kishton, R.J., Nichols, A.G., Macintyre, A.N., Inoue, M., Ilkayeva, O., Winter, P.S., Liu, X., Priyadharshini, B., Slawinska, M.E., et al. (2015). Metabolic programming and PDHK1 control CD4+ T cell subsets and inflammation. J. Clin. Invest. *125*, 194–207. https://doi.org/10.1172/JCI76012.
58. Delgoffe, G.M., Kole, T.P., Zheng, Y., Zarek, P.E., Matthews, K.L., Xiao, B., Worley, P.F., Kozma, S.C., and Powell, J.D. (2009). mTOR differentially regulates effector and regulatory T cell lineage commitment. Immunity *30*, 832–844. https://doi.org/10.1016/j.immuni.2009.04.014.
59. Nagai, S., Kurebayashi, Y., and Koyasu, S. (2013). Role of PI3K/Akt and mTOR complexes in Th17 cell differentiation: Th17 cells and PI3K-Akt-mTOR complexes. Ann. N. Y. Acad. Sci. *1280*, 30–34. https://doi.org/10.1111/nyas.12059.
60. Salmond, R.J. (2018). mTOR regulation of glycolytic metabolism in T cells. Front. Cell Dev. Biol. *6*, 122. https://doi.org/10.3389/fcell.2018.00122.
61. Peng, M., Yin, N., Chhangawala, S., Xu, K., Leslie, C.S., and Li, M.O. (2016). Aerobic glycolysis promotes T helper 1 cell differentiation through an epigenetic mechanism. Science *354*, 481–484. https://doi.org/10.1126/science.aaf6284.
62. Soriano-Baguet, L., and Brenner, D. (2023). Metabolism and epigenetics at the heart of T cell function. Trends Immunol.
63. Hochrein, S.M., Wu, H., Eckstein, M., Arrigoni, L., Herman, J.S., Schumacher, F., Gerecke, C., Rosenfeldt, M., Grün, D., Kleuser, B., et al. (2022). The glucose transporter GLUT3 controls T helper 17 cell responses through glycolytic-epigenetic reprogramming. Cell Metabol. *34*, 516–532.e11. https://doi.org/10.1016/j.cmet.2022.02.015.
64. Brüstle, A., Brenner, D., Knobbe, C.B., Lang, P.A., Virtanen, C., Hershenfield, B.M., Reardon, C., Lacher, S.M., Ruland, J., Ohashi, P.S., and Mak, T.W. (2012). The NF-κB regulator MALT1 determines the encephalitogenic potential of Th17 cells. J. Clin. Invest. *122*, 4698–4709. https://doi.org/10.1172/JCI63528.
65. Cossarizza, A., Chang, H., Radbruch, A., Acs, A., Adam, D., Adam-Klages, S., Agace, W.W., Aghaeepour, N., Akdis, M., Allez, M., et al. (2019). Guidelines for the use of flow cytometry and cell sorting in immunological studies (second edition). Eur. J. Immunol. *49*, 1457–1973. https://doi.org/10.1002/eji.201970107.
66. Battello, N., Zimmer, A.D., Goebel, C., Dong, X., Behrmann, I., Haan, C., Hiller, K., and Wegner, A. (2016). The role of HIF-1 in oncostatin M-dependent metabolic reprogramming of hepatic cells. Cancer Metabol. *4*, 3. https://doi.org/10.1186/s40170-016-0141-0.
67. Hiller, K., Hangebrauk, J., Jäger, C., Spura, J., Schreiber, K., and Schomburg, D. (2009). MetaboliteDetector: comprehensive analysis tool for targeted and nontargeted GC/MS based metabolome analysis. Anal. Chem. *81*, 3429–3439. https://doi.org/10.1021/ac802689c.
68. Lauterbach, M.A., Hanke, J.E., Serefidou, M., Mangan, M.S.J., Kolbe, C.-C., Hess, T., Rothe, M., Kaiser, R., Hoss, F., Gehlen, J., et al. (2019). Toll-like receptor signaling rewires macrophage metabolism and promotes histone acetylation via ATP-citrate lyase. Immunity *51*, 997–1011.e7. https://doi.org/10.1016/j.immuni.2019.11.009.
69. Meiser, J., Tumanov, S., Maddocks, O., Labuschagne, C.F., Athineos, D., Van Den Broek, N., Mackay, G.M., Gottlieb, E., Blyth, K., Vousden, K., et al. (2016). Serine one-carbon catabolism with formate overflow. Sci. Adv. *2*, e1601273. https://doi.org/10.1126/sciadv.1601273.
70. Seim, G.L., Britt, E.C., John, S.V., Yeo, F.J., Johnson, A.R., Eisenstein, R.S., Pagliarini, D.J., and Fan, J. (2019). Two-stage metabolic remodelling in macrophages in response to lipopolysaccharide and interferon-γ stimulation. Nat. Metab. *1*, 731–742. https://doi.org/10.1038/s42255-019-0083-2.
71. Andrews, S. (2010). FastQC: A Quality Control Tool for High Throughput Sequence Data.
72. Schubert, M., Ermini, L., Der Sarkissian, C., Jónsson, H., Ginolhac, A., Schaefer, R., Martin, M.D., Fernández, R., Kircher, M., McCue, M., et al. (2014). Characterization of ancient and modern genomes by SNP detection and phylogenomic and metagenomic analysis using PALEOMIX. Nat. Protoc. *9*, 1056–1082. https://doi.org/10.1038/nprot.2014.063.
73. Kopylova, E., Noé, L., and Touzet, H. (2012). SortMeRNA: fast and accurate filtering of ribosomal RNAs in metatranscriptomic data. Bioinformatics *28*, 3211–3217. https://doi.org/10.1093/bioinformatics/bts611.
74. Dobin, A., Davis, C.A., Schlesinger, F., Drenkow, J., Zaleski, C., Jha, S., Batut, P., Chaisson, M., and Gingeras, T.R. (2013). STAR: ultrafast universal RNA-seq aligner. Bioinformatics *29*, 15–21. https://doi.org/10.1093/bioinformatics/bts635.
75. Patro, R., Duggal, G., Love, M.I., Irizarry, R.A., and Kingsford, C. (2017). Salmon provides fast and bias-aware quantification of transcript expression. Nat. Methods *14*, 417–419. https://doi.org/10.1038/nmeth.4197.
76. Frankish, A., Diekhans, M., Ferreira, A.-M., Johnson, R., Jungreis, I., Loveland, J., Mudge, J.M., Sisu, C., Wright, J., Armstrong, J., et al. (2019).

GENCODE reference annotation for the human and mouse genomes. Nucleic Acids Res. *47*, D766–D773. https://doi.org/10.1093/nar/gky955.

77. Love, M.I., Soneson, C., Hickey, P.F., Johnson, L.K., Pierce, N.T., Shepherd, L., Morgan, M., and Patro, R. (2020). Tximeta: reference sequence checksums for provenance identification in RNA-seq. PLoS Comput. Biol. *16*, e1007664. https://doi.org/10.1371/journal.pcbi.1007664.
78. Love, M.I., Huber, W., and Anders, S. (2014). Moderated estimation of fold change and dispersion for RNA-seq data with DESeq2. Genome Biol. *15*, 550. https://doi.org/10.1186/s13059-014-0550-8.
79. Yu, G., Wang, L.-G., Han, Y., and He, Q.-Y. (2012). clusterProfiler: an R Package for comparing biological themes among gene clusters. OMICS A J. Integr. Biol. *16*, 284–287. https://doi.org/10.1089/omi.2011.0118.
80. Luo, W., and Brouwer, C. (2013). Pathview: an R/Bioconductor package for pathway-based data integration and visualization. Bioinformatics *29*, 1830–1831. https://doi.org/10.1093/bioinformatics/btt285.
81. Corces, M.R., Trevino, A.E., Hamilton, E.G., Greenside, P.G., Sinnott-Armstrong, N.A., Vesuna, S., Satpathy, A.T., Rubin, A.J., Montine, K.S., Wu, B., et al. (2017). An improved ATAC-seq protocol reduces background and enables interrogation of frozen tissues. Nat. Methods *14*, 959–962. https://doi.org/10.1038/nmeth.4396.
82. Adams, M.D., Celniker, S.E., Holt, R.A., Evans, C.A., Gocayne, J.D., Amanatides, P.G., Scherer, S.E., Li, P.W., Hoskins, R.A., Galle, R.F., et al. (2000). The genome sequence of *Drosophila melanogaster*. Science *287*, 2185–2195. https://doi.org/10.1126/science.287.5461.2185.
83. Li, H., Handsaker, B., Wysoker, A., Fennell, T., Ruan, J., Homer, N., Marth, G., Abecasis, G., and Durbin, R.; 1000 Genome Project Data Processing Subgroup (2009). The sequence alignment/map format and SAMtools. Bioinformatics *25*, 2078–2079. https://doi.org/10.1093/bioinformatics/btp352.
84. Stark, R., and Brown, G. (2022). DiffBind: differential binding analysis of ChIP-Seq peak data. Bioconductor *75*. https://doi.org/10.18129/B9.bioc.DiffBind.
85. Amemiya, H.M., Kundaje, A., and Boyle, A.P. (2019). The ENCODE blacklist: identification of problematic regions of the genome. Sci. Rep. *9*, 9354. https://doi.org/10.1038/s41598-019-45839-z.
86. Ramírez, F., Ryan, D.P., Grüning, B., Bhardwaj, V., Kilpert, F., Richter, A.S., Heyne, S., Dündar, F., and Manke, T. (2016). deepTools2: a next generation web server for deep-sequencing data analysis. Nucleic Acids Res. *44*, W160–W165. https://doi.org/10.1093/nar/gkw257.

STAR★METHODS

KEY RESOURCES TABLE

REAGENT or RESOURCE	SOURCE	IDENTIFIER
Antibodies		
Anti-mouse CD4-APC Clone GK1.5	BioLegend	Cat# 100412, RRID:AB_312697
Anti-mouse CD3ε-PE-Cy7 Clone 145-2C11	BioLegend	Cat# 100320, RRID:AB_312685
Anti-mouse CD4-PE Clone GK1.5	BioLegend	Cat# 100408, RRID:AB_312693
Anti-mouse CD4-BV785 Clone GK1.5	BioLegend	Cat# 100453, RRID:AB_2565843
Anti-mouse CD4-BUV737 Clone GK1.5 (RUO)	BD Biosciences	Cat# 612761, RRID:AB_2870092
Anti-mouse IL17A-BV605 Clone TC11-18H10	BD Biosciences	Cat# 564169, RRID:AB_2738640
Anti-mouse IFN-γ-APC Clone XMG1.2	BioLegend	Cat# 505810, RRID:AB_315404
Anti-mouse RORγT-BV421 Clone Q31-378	BD Biosciences	Cat# 562894, RRID:AB_2687545
Anti-mouse Tbet-PE/Cy7 Clone 4B10	BioLegend	Cat# 644824, RRID:AB_2561761
Anti-mouse FoxP3-APC Clone FJK-16	Thermo Fisher Scientific	Cat# 17-5773-82, RRID:AB_469457
Anti-mouse CD25-PE Clone PC61	BioLegend	Cat# 102008, RRID:AB_312857
Anti-mouse pmTOR-PE Clone MRRBY	Thermo Fisher Scientific	Cat# 12-9718-42, RRID:AB_2572724
Anti-mouse pS6-APC Clone cupk43k	Thermo Fisher Scientific	Cat# 17-9007-42, RRID:AB_2573270
Anti-mouse CD45-PerCP/Cyanine5.5 Clone 30-F11	BioLegend	Cat# 103132, RRID:AB_893340
Anti-mouse Glut-1 – Alexa Fluor® 647 Clone EPR3915	Abcam	Cat# ab195020, RRID:AB_2783877
Anti-mouse Hexokinase-1 - Alexa Fluor® 488 Clone EPR10134(B)	Abcam	Cat# ab184818
Anti-mouse CD36-PerCP/Cyanine5.5 Clone HM36	BioLegend	Cat# 102620, RRID:AB_2750188
Ultra-LEAF™ Purified anti-mouse CD3ε Clone 145-2C11	BioLegend	Cat# 100340, RRID:AB_11149115
Ultra-LEAF™ Purified anti-mouse CD28 Clone 37.51	BioLegend	Cat# 102116, RRID:AB_11147170
Purified NA/LE Rat Anti-Mouse IFN-γ Clone XMG1.2	BD Biosciences	Cat# 554408, RRID:AB_395373
Anti-mouse pyruvate dehydrogenase E1-alpha subunit antibody	Abcam	Cat# ab168379
Anti-mouse acetyl-histone H3 antibody	Millipore	Cat# 06–599, RRID:AB_2115283
Anti-mouse actin antibody produced in rabbit	Sigma-Aldrich	Cat# A2066, RRID:AB_476693
Anti-mouse histone H3	Cell Signaling Technology	Cat# 9715S
Anti-mouse acetyl-histone H3 Lys27	Cell Signaling Technology	Cat# 8173S
Mouse anti-rabbit IgG-HRP	Santa Cruz Biotechnology	Cat# sc-2357, RRID:AB_628497
Chemicals, peptides, and recombinant proteins		
PBS (1X) without Ca^{2+}, Mg++, 500mL	Lonza	#BE17-516F
FBS Superior Lot: 0193F	Biochrom GmbH	#S0615
Penicillin-Streptomycin (10,000 U/mL)	Gibco	#11548876
L-Glutamine	Lonza	#BE17-605E
2-Mercaptoethanol	Gibco	#11508916
Methanol	Sigma-Aldrich	#1060351000
Chloroform	Sigma-Aldrich	#34854-1L-M
Ethanol absolute	VWR	#20821.330
Ethanol eurodenatured	VWR	#85823.440
Sodium acetate trihydrate	Sigma-Aldrich	#71188-250MG

(*Continued on next page*)

Continued

REAGENT or RESOURCE	SOURCE	IDENTIFIER
HEPES	Sigma-Aldrich	#H4034-100G
EDTA	Sigma-Aldrich	#EDS-100G
DL-Dithiothreitol solution (DTT)	Sigma-Aldrich	#43816-10ML
BSA	Sigma-Aldrich	#A9647-500G
RPMI 1640 (without L-Glutamine)	Lonza	#BE12-167F
IMDM with HEPES and L-Glutamine	Lonza	#BE12-722F
Collagenase D from *Clostridium histolyticum*	Roche	#11088866001
DNAseI	Sigma-Aldrich	#D4513-1VL
Percoll®	Sigma-Aldrich	#GE17-0891-01
Recombinant human TGF-β	R&D Biosystems	#240-B-002
Mouse IL-6, research grade	Miltenyi Biotec	#130-094-065
Mouse IL-2, research grade	Miltenyi Biotec	#130-098-221
Mouse IL-12, research grade	Miltenyi Biotec	#130-096-707
Cell Trace Violet	Invitrogen	#C34557
Molecular Probes™ 2-NBDG	Invitrogen	#N13195
SYBR™ Fast Green Master Mix	Applied Biosystems™	#4385612
Luna Universal One-Step RT-qPCR Kit	New England BioLabs Inc.	#E3005E
Formaldehyde	Sigma-Aldrich	#252549-1L
Saponin	Sigma-Aldrich	#S4521-25G
DAPI (1:2000)	Invitrogen	#D1306
Zombie NIR™ Fixable Viability Kit	Biolegend	#423106
Zombie Green™ Fixable Viability Kit	Biolegend	#423112
7-AAD	Invitrogen	#A1310
Bodipy™ FL C16	Invitrogen	#D3821
Corning™ Cell-Tak Cell and Tissue Adhesive	Corning™	#354240
Oligomycin A	Sigma-Aldrich	#75351-5MG
FCCP	Sigma-Aldrich	#C2920-10MG
Antimycin A	Sigma-Aldrich	#A8674-25MG
Rotenone	Sigma-Aldrich	#R8875-1G
2-Deoxy-D-glucose	Sigma-Aldrich	#D6134-1G
Sodium pyruvate	Gibco	#12539059
Phorbol 12-myristate 13-acetate (PMA)	Sigma-Aldrich	#P8139-1MG
Calcium ionophore A23187	Sigma-Aldrich	#C7522-1MG
Rapamycin	Invivogen	#tlrl-rap
Torin 1	Sigma-Aldrich	#475991-10MG
SILAC RPMI 1640 Flex Medium	Gibco	#15347143
$^{13}C_6$-glucose	Cambridge Isotope Lab	#CLM-1396
$^{13}C_5$-L-Glutamine	Cambridge Isotope Lab	#CLM-1822-H
$^{13}C_2$-Acetate	Sigma-Aldrich	#282014-250MG
D-(+)-Glucose solution	Sigma-Aldrich	#G8769-100ML
GolgiPlug™ (Protein Transport Inhibitor)	BD Biosciences	#555029
Tween 20	Sigma-Aldrich	#P7949-500ML
NaCl	Sigma-Aldrich	#S9888-5KG
Sodium bicarbonate solution	Sigma-Aldrich	#S8761-100ML
Protease/Phosphatase Inhibitor Cocktail (100x)	Cell Signaling Technology	#5872
Powdered milk	Carl Roth	#T145.2
Luminata™ Crescendo Western HRP substrate	Merck Millipore	#WBLUR0100
Seahorse XF DMEM medium	Agilent Technologies	#103575-100
Critical commercial assays		
$CD4^+$ T cell Isolation Kit	Miltenyi Biotec	#130-104-454

(*Continued on next page*)

Continued

REAGENT or RESOURCE	SOURCE	IDENTIFIER
Naive CD4$^+$ T cell Isolation Kit, mouse	Miltenyi Biotec	#130-104-453
NucleoSpin RNA 250	Macherey-Nagel	#740955.250
Foxp3/Transcription Factor Staining Buffer Set	Invitrogen	#00-5521-00
BD Cytofix/Cytoperm Fixation/Permeabilization kit	BD Biosciences	#554714
Mouse IL17 DuoSet ELISA	R&D Systems	#DY421
Seahorse XFe96 Fluxpak	Agilent Technologies	#102416-100
EAE induction kit: MOG35-55/CFA Emulsion PTX	Hooke Laboratories, Inc	#EK-2110
Deposited data		
RNA-seq	This manuscript	GEO: GSE222882
ATAC-seq	This manuscript	GEO: GSE222882
Experimental models: Organisms/strains		
Mouse: B6.129P2-Pdha1^{tm1Ptl}/J	Jackson Laboratory	JAX: 17,443, RRID:IMSR_JAX:017,443
Mouse: B6.Cg-Tg(Cd4-cre)1Cwi/BfluJ	Jackson Laboratory	JAX: 022,071, RRID:IMSR_JAX:022,071
Oligonucleotides		
Tbp Forward: GAAGAACAATCCAGACTAGCAGCA	Kurniawan et al., 2020[56]	N/A
Tbp Reverse: CCTTATAGGGAACTTCACATCACAG	Kurniawan et al., 2020[56]	N/A
Pdha1 Forward: CGT CTG TTG AGA GAG CAG CA	This manuscript	N/A
Pdha1 Reverse: CGC ACA AGA TAT CCA TTC CA	This manuscript	N/A
Pdhb Forward: AGGAGGGAATTGAATGTGAGGT	This manuscript	N/A
Pdhb Reverse: ACTGGCTTCTATGGCTTCGAT	This manuscript	N/A
Recombinant DNA		
Plasmid: pMIT-Pdha1-CD90.1	This manuscript	N/A
Plasmid: pMIT-CD90.1	This manuscript	N/A
Software and algorithms		
FlowJo Software	Tree Star	RRID:SCR_008520
Graphpad Prism	GraphPad Software, Inc	RRID:SCR_002798
Wave Software	Agilent	RRID:SCR_014526
Inkscape	Inkscape	RRID:SCR_014479

RESOURCE AVAILABILITY

Lead contact

Further information and requests for resources or reagents should be directed to and will be made available upon reasonable request by the Lead Contact, Dirk Brenner (dirk.brenner@lih.lu).

Materials availability

All unique/stable reagents generated in this study are available from the lead contact without restriction.

Data and code availability

- RNA-seq and ATAC-seq data have been deposited at GEO and are publicly available as of the date of publication. Accession number is listed in the key resource table. All other data reported in this paper will be shared by the lead contact upon request.
- This paper does not report original code.
- Any additional information required to reanalyze the data reported in this paper is available from the lead contact upon request.

EXPERIMENTAL MODEL AND SUBJECT DETAILS

Mice

PDH$^{fl/fl}$ mice [B6.129P2-Pdha1tm1Ptl/J] were purchased from The Jackson Laboratory and crossed with CD4 Cre-expressing mice, also obtained from The Jackson Laboratory. All experiments used sex- and age-matched mice (8–12 weeks old) with corresponding littermate controls. Male and female mice were used in all *in vitro* experiments.

EAE mouse model

Induction of EAE was performed and clinical scores determined based on the neurological signs described in Table S1.[64] Briefly, $PDH^{fl/fl}$ and $PDH^{fl/fl}$ CD4 Cre + male mice were injected subcutaneously with MOG_{35-55}/CFA emulsion, followed by two intraperitoneal injections of pertussis toxin (Hooke Labs). Mouse brains and spleens were analyzed at day 14 post-induction.

Study approval

All animal experimentation protocols were approved and conducted according to the LIH Animal Welfare Structure guidelines.

METHOD DETAILS

Naive T cell isolation from spleen and lymph nodes

Naive $CD4^+$ T cells were isolated from $PDH^{fl/fl}$ and $PDH^{fl/fl}$ CD4 Cre + mouse spleen and lymph nodes by magnetic bead sorting (MACS) using the Naive $CD4^+$ T cell isolation kit (Miltenyi Biotec) according to the manufacturer's protocol. Sorting was performed using an autoMACS pro-Separator (Miltenyi Biotec). Cell number calculations were performed using a CASY cell counter (Omni Life Science).

Isolation of lymphocytes from mouse brain

Isolation of lymphocytes from the brains of EAE-affected mice at day 14 post-induction was performed.[64] Mice were sacrificed and brains were perfused with 20 mL cold PBS through the left ventricle. Brains were digested in RPMI supplemented with 50 μg/mL collagenase D (Roche) and 10 μg/mL DNAse I (Sigma-Aldrich) for 1 h at 37°C in a mixer (Labortechnik). Lymphocyte enrichment was obtained by centrifugation using a two-layer Percoll gradient (40% and 70%), followed by two washes in RPMI.

In vitro differentiation of Th cell subsets

Naive T cells isolated from $PDH^{fl/fl}$ and $PDH^{fl/fl}$ CD4 Cre + spleen and lymph nodes as described above were seeded at $2x10^6$ cells/mL in complete medium consisting of IMDM (Lonza) supplemented with 10% FBS (Biochrom GmbH), 55μM 2-mercaptoethanol (Gibco) and 1% penicillin/streptomycin (Gibco), and incubated for 3 days in the presence of the appropriate Th subset-specific cytokine mix (cf. Table S2). For acetate-treated cells, *in vitro* Th cell differentiation was performed in the presence of 10 mM sodium acetate (Sigma-Aldrich) diluted in culture medium. For experiments examining the effects of glutamine, cells were cultured in RPMI-1640 medium (Lonza) supplemented with 10% FBS (Biochrom GmbH), 55μM 2-mercaptoethanol (Gibco) and 1% penicillin/streptomycin (Gibco) with 1% L-Glutamine (Lonza) (Complete) or without glutamine (w/o Glutamine).

Immunoblotting

Cells were lysed in lysis buffer (Cell Signaling Technology, 9803S) containing protease and phosphatase inhibitors (Cell Signaling Technology) following manufacturer's instructions. 20 μL of lysates were loaded on 16% polyacrylamide gels (Invitrogen), followed by electrophoresis and transfer to membrane.[56] The antibodies used for protein detection were anti-Pdha1 (Abcam, ab168379), anti-actin (Sigma Aldrich), anti-acetyl-histone H3 Lys27 (Cell Signaling Technology, 8173S), anti-histone H3 (Cell Signaling Technology, 9715S) and anti-acetyl-histone H3 (Millipore, 06–599) all diluted 1:1000 in TBS-T.

Flow cytometry

For the detection of surface markers, cells were stained for 30 min at 4°C in FACS buffer (PBS with 1% fetal bovine serum (FBS; Gibco) and 5 mM EDTA, pH 8.0) containing antibodies (cf. key resources table; 1:200 dilution) and one of four viability dyes: DAPI (Invitrogen), LIVE/DEAD Fixable Near-IR or Green Dye (Biolegend), or 7-AAD (Invitrogen; 1:1000-1:3000 dilution). Cells were washed in FACS buffer before flow cytometry measurements.

For intracellular staining of transcription factors, cells were fixed at 4°C for 1hr using the eBioscience FoxP3/Transcription Factor Fixation kit (Invitrogen) and permeabilized using the buffer provided by the kit. To measure intracellular cytokine expression, cells were restimulated for 5hr *in vitro* with phorbol 12-myristate 13-acetate (PMA; Sigma, 50 ng/mL), calcium ionophore A23187 (Ionomycin, Sigma, 750 ng/mL), and BD GolgiPlug Protein Transport Inhibitor (BD Biosciences, 1:1000 dilution). Cells were washed once with FACS buffer before extracellular staining, then fixed for 20 min at 4°C with BD Cytofix/Cytoperm and permeabilized with BD Perm/Wash buffer (BD Biosciences). To detect hexokinase-1, cells were fixed in 4% formaldehyde (Sigma-Aldrich) for 10 min at room temperature (RT), then permeabilized in PBS containing 0.1% Tween 20. For p-mTOR and p-S6 detection, cells were fixed in 2% formaldehyde (Sigma-Aldrich) for 10 min at RT, then permeabilized in 0.01% saponin (Sigma-Aldrich). Antibodies used for intracellular staining were diluted 1:200 in the appropriate permeabilization buffer prior to incubation with cells for 30 min at 4°C.

To measure 2-NBDG uptake, cells were incubated in glucose-free RPMI for 2 h at 37°C in the presence of 50 μM 2-NBDG (Invitrogen). To measure lipid uptake, cells were incubated in IMDM containing 1 μM BODIPY FL C16 (Invitrogen) for 30 min at 37°C. Cells were washed once with PBS prior to flow cytometric measurements.

Experiments have been done in accordance with the guidelines for flow cytometry and cell sorting.[65] All flow cytometric measurements were obtained using a BD Fortessa instrument (BD Biosciences) and analyses were performed using FlowJo v10.6.2 software (Tree Star).

Expression plasmids and retroviral transduction

Murine full-length *Pdha1* cDNA was cloned into the pMIT-CD90.1 vector at the EcoRI restriction site (GeneCust, France), with empty pMIT-CD90.1 vector serving as the control. Retroviral transduction was performed by adding retroviral supernatants to *in-vitro* differentiated Th17 cells on day 1 by spin infection.[55,56] Infected cells were cultured at 37°C in the appropriate Th subset differentiation medium for 48h, followed by MACS-sorting using the CD90.1 marker.

Cytokine quantification

Measurement of IL-17 in culture supernatants of *in vitro*-differentiated Th17 cells was performed using the Mouse IL-17 DuoSet ELISA kit (R&D Systems) following the manufacturer's instructions.

ATP quantification

ATP levels in $1x10^5$ *in vitro*-differentiated Th17 cells were measured using the CellTiter-Glo assay (Promega) according to the manufacturer's protocol.

Metabolic flux measurements and analysis

In vitro-differentiated Th17 cells were seeded at $3x10^5$ cells/well in a pre-coated XFe96 cell culture plate (Agilent Technologies) using Corning Cell-Tak Cell and Tissue Adhesive (Corning) and 0.1 M sodium bicarbonate (Sigma-Aldrich).

For OCR measurements, plated cells were cultured in XF Seahorse DMEM medium (Agilent Technologies) containing 2 mM glutamine (Lonza), 1 mM sodium pyruvate (Gibco) and 25 mM glucose (Sigma-Aldrich). OCR was measured using the XF Cell Mito Stress Test (Agilent Technologies) following the manufacturer's protocol, which involved sequential injections of oligomycin A (1 μM), carbonyl cyanide 4-(trifluoromethoxy)phenylhydrazone (FCCP; 3 μM) and antimycin A/rotenone (1 μM) (all from Sigma-Aldrich).

For ECAR measurements, plated cells were cultured in XF Seahorse DMEM medium (Agilent Technologies) containing 2 mM glutamine (Lonza), and ECAR was determined by the XF Glycolysis Stress Test Kit (Agilent Technologies). Measurements were taken during sequential injections of glucose (10 mM), oligomycin (1 μM) and 2-deoxy-D-glucose (2-DG; 50 mM) (all from Sigma-Aldrich).

Experiments were performed using an XFe96 Extracellular Flux Analyzer (Agilent), and results were analyzed using Wave 2.6.1 software (Agilent Technologies). All measurements were calculated from raw OCR or ECAR data as described in Table S3.

Isotopic labeling

For glucose and glutamine isotopic tracing, naive T cells were incubated for 3 days with the appropriate cytokine cocktail to induce Th cell differentiation *in vitro*. At day 3, cells were counted, washed and seeded for 24hr in tracing medium consisting of SILAC RPMI 1640 (Gibco) supplemented with 10% FBS (Biochrom GmbH), 55μM 2-mercaptoethanol (Gibco), 1% penicillin/streptomycin (Gibco), L-arginine (Sigma-Aldrich) and L-lysine (Sigma-Aldrich), and containing [U-$^{13}C_6$]-glucose (11.1 mmol/L; Cambridge Isotope Laboratories) or [U-$^{13}C_5$]-glutamine (2 mmol/L; Cambridge Isotope Laboratories).

For acetate isotopic tracing, naive T cells were incubated for 3 days in complete IMDM medium containing the appropriate cytokine cocktail and [U-$^{13}C_2$]-acetate (10 mM; Sigma-Aldrich).

Extraction of intracellular metabolites, MID and carbon contribution determinations, GC and LC-MS measurements, and substractions of natural isotope abundance, were performed using MetaboliteDetector software.[66] Glucose, lactate and glutamine concentrations in medium were measured by a YSI 2950D Biochemistry Analyzer (YSI Incorporated).

GC-MS measurement of non-polar fractions, data processing and normalization

Derivatization was performed using a multi-purpose sample preparation robot (Gerstel). Dried non-polar extracts of ^{13}C-glucose or ^{13}C-glutamine treated Th17 cells were dissolved in 30 μL N-Methyl-N-(tert-butyldimethylsilyl)trifluoroacetamide (MTBSTFA) containing 1% tert-butyldimethylchlorosilane (TBDMCS) and incubated for 60 min at 55°C with continuous shaking.

GC-MS analysis was performed using an Agilent 7890A GC coupled to an Agilent Mass Selective Detector (MSD; Agilent Technologies). A sample volume of 1 μL was injected into a Split/Splitless inlet operating in splitless mode at 280°C. The gas chromatograph was equipped with a 30 m (I.D. 0.25 mm, film 0.25 μm) ZB-5MSplus capillary column (Phenomenex) with a 5 m guard column in front of the analytical column. Helium was used as the carrier gas with a constant flow rate of 1.4 mL/min. GC temperature program was 100°C for 1 min, then increased to 325 °C at 7.5 °C/min, and held for 4 min. The total run time was 35 min. The transfer line temperature was set to 280°C. The MSD was operating under electron ionization at 70 eV. The MS source was held at 230°C and the quadrupole at 150°C. GC-MS measurements were performed in selected ion monitoring mode for precise determination of MIDs.

MetaboliteDetector (v3.2.20190704) was used to process all GC-MS chromatograms.[67] Compounds were annotated by retention time and mass spectrum using an in-house mass spectral library (overall similarity: >0.85). The following deconvolution settings were

applied: Peak threshold of 2; Minimum peak height of 2; 10 Bins per scan; Deconvolution width of 8 scans; No baseline adjustment; Minimum 1 peak per spectrum; No minimum required base peak intensity. MIDs for the following fragments were calculated (cf. Table S4).

LC-MS analysis of histones

Histones were extracted using acid extraction and separated on a 16% polyacrylamide gel.[68] In-gel acylation of histones was performed using propionic anhydride. Subsequently, in-gel digestion of histone proteins was performed to obtain tryptic-digested peptides. Peptides were desalted using C18-Omix tips (Agilent Technologies), vacuum-dried, and reconstituted in 0.1% formic acid in water. Peptide digest (10 μL) was injected into a Vanquish UHPLC System (Thermo Scientific) equipped with Hypersil GOLD and coupled to an Orbitrap ID-X Tribrid Mass Spectrometer (Thermo Scientific). Peptides were separated on Vanquish C18 UHPLC Columns (150*2.1 mm, 1.9 μm) at a flow rate of 300 μL/min using a 50 min gradient program starting from 5% to 50% of mobile phase B, where mobile phase A was water containing 0.1% formic acid and mobile phase B was acetonitrile containing 0.1% formic acid. The MS instrument was operated in full scan mode (m/z 350–1600) with resolution R = 60,000 at m/z 400. Peptide fragmentation was performed using data-dependent acquisition (DDA). The top 10 peptide ions subjected to DDA-based ms/ms fragmentation were selected based on peptide ions' intensity. Typical mass spectrometric conditions were as follows: AGC target, standard; spray voltage, 4000 V; 45; auxiliary gas flow, 10; ion transfer tube temperature, 325°C; vaporizer temperature, 325°C; DDA cycle time, 3; collision energy, 30%. Tracefinder software was used for manual inspection of chromatograms and integration of peak areas. Peptide identification and confirmation were performed using Skyline software.

GC-MS of samples labeled by ^{13}C-palmitate

From the polar phase of ^{13}C-palmitate treated Th17 cells, 250 μL were transferred to a glass vial with a micro insert and lyophilized in a CentriVap (Labconco Corporation). The metabolites in the polar phase were derivatized before injection into the GC-MS system. To this end, 15 μL methoxyamine hydrochloride (20 mg/mL in pyridin) were injected into the glass vials and incubated at 55°C for 30 min, followed by injection of 15 μL MTBSTFA and further derivatization for 90 min. For quantification of labeled palmitate, 500 μL derivatization reagent [2% (v/v) H_2SO_4 in methanol] was added to the dried non-polar phase. The samples were incubated for 2 h at 50°C. Subsequently, 100 μL saturated NaCl solution and 500 μL hexane were added to the reaction tube, followed by vortexing for 2 min. After phase separation, 400 μL of the upper hexane phase was collected in a new reaction tube. An additional 500 μL hexane were added to the first reaction tube and the previous steps were repeated. After evaporating the hexane from the second reaction tube in a CentriVap, the samples were reconstituted in 75 μL hexane and transferred to a glass vial with micro insert and capped immediately.

For analysis of polar metabolites, 1 μL sample was injected into an SSL injector at 270°C in splitless mode. GC-MS analysis was performed using a 7890A GC System from Agilent coupled to a 5975C inert XL MSD. The GC was equipped with a 30 m ZB-35 column from Zebron and helium was used as a carrier gas with a flow rate of 1 mL/min. The initial oven temperature of 100°C was held for 2 min, followed by an increase in temperature to 300 °C at a rate of 10 °C/min, which was held for 4 min. Metabolites were detected in selected ion monitoring (SIM) mode. The MSD was operating under electron ionization at 70 eV.

For fatty acid analysis, 1 μL sample was injected into an SSL injector at 270°C in splitless mode. GC-MS analysis was performed using a 7890A GC System from Agilent coupled to a 5975C inert XL MSD. The GC was equipped with a VF-35 MS column from Agilent and helium was used as a carrier gas with a flow rate of 1 mL/min. The initial oven temperature of 55°C was held for 5 min, followed by an increase in temperature to 325 °C at a rate of 6 °C/min, which was held for 10 min. Metabolites were detected in full scan mode and mass spectra were acquired from *m/z* 70 to 800. The MSD was operating under electron ionization at 70 eV.

Data analysis of relative metabolite levels and analysis of mass isotopomer distribution (MID) were performed using Metabolite Detector software.[67]

Acetyl-CoA measurement by LC-MS

The LC-MS setup consisted of a Vanquish Flex (Thermo Scientific) liquid chromatography system configured in binary gradient coupled to a Q-Exactive Plus mass spectrometer (Thermo Scientific). The analytical column was a SeQuant ZIC-pHILIC (Merck) (2.1 mm × 150 mm, 5 μm) with a guard column (2.1 mm × 20 mm), and was heated at 45°C in the column oven. Solvent A was 20mM ammonium carbonate (pH 9.2) containing 5μM medronic acid. Solvent B was pure acetonitrile. Samples were injected onto the column and eluted using a linear gradient that ranged from 80% Solvent B to 20% Solvent B, and was conducted over 15 min at a constant flow rate of 200 μL/min.

Acetyl-CoA isotopic enrichment was measured by selected ion monitoring (SIM). The quadrupole isolation window was set from 808 to 838 m/z in order to accumulate all the isotopologues of acetyl-CoA, from the M+0 (810.1331 m/z) to the M+23 (833.2102 m/z). The maximum accumulation time was set to 250 ms, with automatic gain control of 1e6 charges. Orbitrap resolution was set to 140,000 at 200 m/z. Data was acquired with Thermo Xcalibur software (Version 4.3.73.11) and analyzed with TraceFinder (Version 4.1). Subsequent data analysis for normalization and natural isotope subtraction were performed using in house script.[69]

For calculations of isotopic distributions of acetyl groups in acetyl-CoA, the formulas described by Seim et al. were applied but, instead of using the MIDs for CoA, the MIDs of ATP were used.[70]

Proliferation

Cells ($1x10^6$) were labeled with 5μM CellTrace Violet (CTV; Invitrogen) for 72hr and analyzed by flow cytometry according to the manufacturer's protocol. Division indexes were calculated using FlowJo software.

RNA extraction and quantitative RT-PCR

RNA was extracted using a NucleoSpin RNA Kit (Macherey-Nagel) according to the manufacturer's protocol. RNA concentrations were measured by a NanoDrop 2000c Spectrophotometer (Thermo Fisher Scientific). RT-qPCR was carried out by mixing 2μL RNA (150 ng) with 5μL Master Mix (Luna Universal One-Step RT-qPCR Kits; New England BioLabs Inc.), 2pmol forward primer, 2pmol reverse primer, 0.3μL reverse transcriptase and 2.7μL RNAse-free water (cf. key resources table). Reactions were run on a CFX384 instrument (Bio-Rad). Data were normalized to *Tbp* gene (housekeeping) and analyzed using the ΔΔCt method.[55]

RNA-seq sample preparation

RNA was extracted as described above. RNA-seq and ATAC-seq were performed on the same pools of $PDH^{fl/fl}$ and $PDH^{fl/fl}$CD4 Cre + naive T cells induced to differentiate into Th17 cells *in vitro* for 72 h mRNA sequencing was performed by the Sequencing Platform of the Luxembourg Center for Systems Biomedicine (LCSB) of the University of Luxembourg. Single-end (RNA-seq samples round 1) or paired-end (RNA-seq samples round 2), stranded sequencing was executed using an Illumina NextSeq 500 machine with a read length of 75 bp. The TruSeq Stranded mRNA Library Prep kit (Illumina) was used for library preparation.

RNA-seq data analysis

FastQC (v0.11.5) was used to assess the quality control of the raw reads.[71] Adapter removal was performed using the PALEOMIX pipeline (v1.2.12),[72] with a minimum length of the remaining reads set to 25 bp. SortMeRNA (v2.1) was used to remove rRNA reads,[73] followed by mapping using STAR (v.2.5.2b).[74] RNA-seq transcript alignment was performed with Salmon[75] against the Mouse Transcriptome from Genecode v.M30.[76] Subsequent analysis was conducted in R, and Tximeta[77] was used to assign transcripts to genes before differential analysis with DESeq2.[78] Gene set enrichment analysis (GSEA) was performed using ClusterProfiler.[79] Colored KEGG view pathways were prepared using Pathview.[80]

ATAC-seq sample preparation

RNA-seq and ATAC-seq were performed on the same pools of $PDH^{fl/fl}$ and $PDH^{fl/fl}$ CD4 Cre + naive T cells induced to differentiate into Th17 cells *in vitro* for 72 h. ATAC-seq was performed using OMNI-ATAC supplementary protocol 1 by Corces et al.[81] with some modifications. Viable cells ($1x10^5$) were resuspended in 50 μL cold ATAC-Resuspension Buffer (RSB) containing 0.1% NP40, 0.1% Tween 20 and 0.01% digitonin, and lysed for 3 min on ice. Lysates were washed with 1 mL cold ATAC-RSB containing 0.1% Tween 20 but no NP40 or digitonin. Samples were centrifuged for 10 min at 500×g at 4°C, the supernatants removed, and the pellets resuspended in 50 μL transposition mix (Tagment DNA buffer from Illumina, #15027866) containing 2.5 μL Tagment DNA TDE1 Enzyme (Illumina #15027865). After 45 min incubation at 37°C and 1000 rpm in an Eppendorf ThermoMixer, chromatin fragments were isolated using the Zymo Research DNA Clean & Concentrator kit (ZymoResearch ZY-D4013). For pre-amplification of transposed fragments, 5 PCR cycles were run using primers Ad1 and Ad2.x.[35] The remaining cycles of library amplification were determined by qPCR.[82] Another clean-up was performed using the Zymo Research DNA Clean & Concentrator kit (21 μL elution volume) followed by size selection using AMPure XP beads (Beckman Coulter #A63880), with samples adjusted to 100 μL plus 55 μL of beads to remove large fragments. Samples were incubated for 5 min before bead separation using a magnetic stand and transfer of the supernatant to a new tube. Another 225 μL of beads were added followed by incubation for 10 min and separation on a magnetic stand. After washing with 80% ethanol, beads were resuspended in 20 μL elution buffer and incubated for 5 min. After separation on a magnetic stand, the eluate was transferred to a new tube. Library quality control was performed using the Agilent DNA High Sensitivity Bioanalyzer chip (Agilent #5067-4626). The sequencing of ATAC-seq libraries was performed by the Sequencing Platform of LCSB. Paired-end, unstranded library sequencing was performed using the Illumina NextSeq 500/550 75 cycles High Output Kit.

ATAC-seq data analysis

FastQC (v0.11.5) was used to assess the quality control of raw reads.[71] Alignment and mapping to generate BAM files were performed with BWA (v.0.7.16a).[83] The mouse reference genome used for mapping was GRCm38 release 102 downloaded from GENCODE (https://www.gencodegenes.org/). The Picard tool (v2.10.9)[82] was used to validate BAM files. Genrich (https://github.com/jsh58/Genrich) was used for peak calling with parameters "-r -m 30 -j -a 200 -g 15 -L 15 -d 50" to remove PCR duplicates and include only reads with mapping quality of at least 30. This approach also achieved a minimum AUC for a peak of 200 bp, a maximum distance between significant sites of 15 bp, a minimum length of a peak of 15 bp, and cut sites to 50 bp.

Samples for ATAC-seq with more than 15 million read were kept for analysis. Differentially accessible regions were detected using DiffBind (3.6.1)[84] in R (4.2.0). Briefly, peaks from all samples have been overlapped and merged resulting into 132,759 unique regions. Then, a blacklist region obtained from the ENCODE[85] project was applied to filter out problematic regions resulting into 116,364 peaks that were identified in at least two samples and constituted the peakset. Then, the number of mapped reads was calculated for each peak included in the peakset and background normalization was performed. Finally, differential analysis was performed using DESeq2 resulting into 39,647 significant regions with differentially opened chromatin between the $PDH^{fl/fl}$ and $PDH^{fl/fl}$ CD4

Cre + untreated conditions using an adjusted p value of 0.05. ATAC-seq tracks were generated using the bamCoverage command from deepTools (3.5.1)[86] with the –scaleFactor setting enabled and being equaled to the normalization factors as calculated by DESeq2 for each sample.

QUANTIFICATION AND STATISTICAL ANALYSIS

Data are presented as the mean ± SEM with a minimum n = 3 per group (for more information, please refer to the Figure Legends). p values were calculated using the unpaired Student's t test, or one or two-way ANOVA using Tukey test correction for multiple comparisons, and Prism 9.3.1 (GraphPad). Statistical significance was set at $p \leq 0.05$, with levels indicated by asterisks as follows: *$p \leq 0.05$; **$p \leq 0.01$; ***$p \leq 0.001$; ****$p \leq 0.0001$; ns, not significant.